Measurement of B^+, B^0 and Λ^0_b production in pPb collisions at $\sqrt{s_{NN}} = 8.16$ TeV

LHCb Collaboration

Measurement of B^+, B^0 and Λ_b^0 production in pPb collisions at $\sqrt{s_{\mathrm{NN}}} = 8.16$ TeV

R. Aaij *et al.*[*]

(LHCb Collaboration)

The production of B^+, B^0 and Λ_b^0 hadrons is studied in proton-lead collisions at a center-of-mass energy per nucleon pair of $\sqrt{s_{\mathrm{NN}}} = 8.16$ TeV recorded with the LHCb detector at the LHC. The measurement uses a dataset corresponding to an integrated luminosity of 12.2 ± 0.3 nb^{-1} for the case where the proton beam is projected into the LHCb detector (corresponding to measuring hadron production at positive rapidity) and 18.6 ± 0.5 nb^{-1} for the lead beam projected into the LHCb detector (corresponding to measuring hadron production at negative rapidity). Double-differential cross sections are measured and used to determine forward-backward ratios and nuclear modification factors, which directly probe nuclear effects in the production of beauty hadrons. The double-differential cross sections are measured as a function of the beauty-hadron transverse momentum and rapidity in the nucleon-nucleon center-of-mass frame. Forward-to-backward cross section ratios and nuclear modification factors indicate a significant nuclear suppression at positive rapidity. The ratio of Λ_b^0 over B^0 production cross sections is reported and is consistent with the corresponding measurement in pp collisions.

I. INTRODUCTION

Charm and beauty quarks provide a unique probe of nuclear matter in heavy-ion collisions [1]. They are produced at early times of the collisions and experience the whole evolution of the nuclear medium before hadronization [2]. Their kinematics and hadronization provide information on the extent of thermalization effects and on transport coefficients. The hard scale provided by the heavy-quark mass is larger than the quantum chromodynamics (QCD) scale, Λ_{QCD}. Therefore, heavy-quark production can be addressed with perturbative QCD down to zero transverse momentum (p_{T}).

The characterization of the extended color-deconfined thermodynamic system, the quark-gluon plasma, using heavy-quark observables in heavy nucleus-nucleus collisions, requires an understanding of background effects. Therefore, it is mandatory to identify and constrain other QCD effects that may appear in nuclear collisions. Among these effects, the modification of the parton distribution functions [3–7] or, alternatively, the breakdown of collinear factorization in the gluon-dense nuclear wave function [8,9] are discussed most extensively. Besides the modification of

the nuclear wave function compared to that of free nucleons, coherent gluon radiation at small angles may modify final-state heavy-quark kinematic distributions [10]. Furthermore, the nuclear effect that is responsible for the change of hadronization patterns as a function of final-state particle multiplicities in small collision systems (pp and proton-nucleus collisions), first observed for strange-hadron production [11], is not yet fully understood. Measurements sensitive to hadronization fractions in the heavy-flavor sector can contribute to a better understanding. Studies of hadronization in heavy nuclear collisions may help to explain the puzzle of heavy-flavor hadron collective behavior that was observed recently in pp and proton-lead collisions [12–14]. These measurements in small collision systems still require a common reconciliation with the global theoretical picture of heavy-ion collisions based on fluid dynamics, or might result in modifications to the fluid-based description.

Observables related to charm hadrons have been extensively studied at the high-energy frontier of heavy-ion collisions at RHIC and the LHC [1]. Recently, the first measurements of Λ_c^+ baryon[1] production in proton-lead collisions have been performed at the LHC [15,16]. The measurements of charm-baryon production were the last important step toward the evaluation of the total charm production cross section without relying on assumptions

---

---

[1]The inclusion of charge-conjugated state is implicit throughout unless explicitly noted.

about charm fragmentation functions based on measurements made before the start of the LHC.[2] Beauty hadrons are not yet explored experimentally to the same extent in heavy-ion collisions due to lower production rates. Theoretically, computations of the production of beauty hadrons are more reliable than charm hadrons since the larger beauty-quark mass allows for a better separation of energy scales with respect to Λ_{QCD}. The LHCb collaboration has recently studied the production of J/ψ mesons from beauty-hadron decays (nonprompt J/ψ) in proton-lead collisions [17]. This measurement is sensitive to beauty-quark production down to vanishing transverse momentum with good precision.

This article presents measurements of the production cross sections of fully reconstructed B^+, B^0 and Λ_b^0 hadrons in proton-lead collisions recorded by the LHCb experiment, as a function of the hadron kinematics down to $p_{\text{T}} = 2$ GeV/c, which is lower than the hadron masses. The measurement of heavy-quark production at low p_{T} helps to constrain the gluon wave function in the nucleus in the small Bjorken x region [18–21], where x is the fraction of the nucleon momentum carried by the interacting gluon. In addition, production measurements of fully reconstructed beauty hadrons in heavy-ion collisions can test whether the hadronization fractions in nuclear collisions are the same as those measured in pp collisions [22–25].

II. DETECTOR, DATA SAMPLES AND OBSERVABLES

The LHCb detector [26,27] is a single-arm forward spectrometer covering the pseudorapidity range $2 < \eta < 5$, designed for the study of particles containing b or c quarks. The detector includes a high-precision tracking system consisting of a silicon-strip vertex detector (VELO) surrounding the initial beam interaction region [28], a large-area silicon-strip detector located upstream of a dipole magnet with a bending power of about 4 Tm, and three stations of silicon-strip detectors and straw drift tubes [29] placed downstream of the magnet. The tracking system provides a measurement of the momentum, p, of charged particles with a relative uncertainty that varies from 0.5% at low momentum to 1.0% at 200 GeV/c. The minimum distance of a track to a primary vertex (PV), the impact parameter (IP), is measured with a resolution of $(15 + 29/p_{\text{T}})$ μm, where p_{T} is in GeV/c. Different types of charged hadrons are distinguished using information from two ring-imaging Cherenkov detectors [30]. Photons, electrons and hadrons are identified by a calorimeter system consisting of scintillating-pad and preshower detectors, an electromagnetic calorimeter and a hadronic calorimeter. Muons are identified by a system composed of

---

[2]Other charm baryons have a negligible contribution to the total charm production.

alternating layers of iron and multiwire proportional chambers [31].

The online event selection is performed by a trigger [32], which consists of a hardware stage, based on information from the calorimeter and muon systems, followed by a two-stage software trigger. The first stage of the software trigger selects displaced high-p_{T} tracks or pairs of high-p_{T} muons, while the second stage searches for $\mu^+\mu^-$ pairs consistent with J/ψ decays and two-, three- or four-track secondary vertices with a full event reconstruction. Between the two stages of the software trigger, an alignment and calibration of the detector is performed in near real-time [33] and updated constants are made available for the trigger reconstruction. The same alignment and calibration information is propagated to the offline reconstruction, ensuring consistent and high-quality particle identification (PID) information between the trigger and offline software. The identical performance of the online and offline reconstruction offers the opportunity to perform physics analyses directly using the $\mu^+\mu^-$ pairs reconstructed in the trigger [32,34], which the present analysis also exploits.

Simulation is required to model the effects of the detector geometrical acceptance and the efficiency of the selection requirements. In the simulation, minimum bias proton-lead collisions are generated using the EPOS LHC generator [35]. Beauty hadrons (H_b) are generated in pp collisions at the same center-of-mass energy using PYTHIA8 [36,37] and are embedded in the minimum bias proton-lead collision events. Decays of particles are described by EVTGEN [38], in which final-state radiation is generated using PHOTOS [39]. The interaction of the generated particles with the detector, and its response, are implemented using the GEANT4 toolkit [40] as described in Ref. [41].

The measurement of the production of beauty hadrons in this analysis uses data recorded in 2016 during the LHC proton-lead run at a center-of-mass energy per nucleon pair of $\sqrt{s_{\text{NN}}} = 8.16$ TeV. The measurement is performed in bins of beauty-hadron p_{T} and rapidity, y. The rapidity is defined in the nucleon-nucleon center-of-mass frame, using the proton beam direction as the direction of the z-axis of the coordinate system. Since the energy per nucleon in the proton beam is larger than in the lead beam, the nucleon-nucleon center-of-mass system has a rapidity in the laboratory frame of 0.465. During the data taking in 2016, the LHC provided collisions with two configurations, inverting the direction of the proton and lead beams. The LHCb forward spectrometer covers the positive (negative) rapidity ranges when the proton (lead) beam direction is projected into the detector from the interaction region, denoted as "pPb" ("Pbp") configuration.

The dataset corresponds to an integrated luminosity of 12.2 ± 0.3 nb^{-1} for the pPb configuration and 18.6 ± 0.5 nb^{-1} for the Pbp configuration, calibrated using dedicated luminosity runs [42]. The double-differential cross

section of the production of a H_b hadron as a function of p_T and y is computed as

$$\frac{d^2\sigma(H_b)}{dp_T dy} \equiv \frac{N(H_b) + N(\bar{H}_b)}{\mathcal{B}(H_b) \cdot \mathcal{L} \cdot \epsilon \cdot \Delta p_T \cdot \Delta y} \qquad (1)$$

where, for a given interval of p_T and y, $N(H_b) + N(\bar{H}_b)$ is the sum of the observed signal yields in a particular decay mode and its charge-conjugated decay mode, $\mathcal{B}(H_b)$ is the product of the branching fractions for the beauty decay and the subsequent charm decay, $\mathcal{L}$ is the integrated luminosity, and ϵ is the total detection efficiency of the final state particles. The measurements are carried out in the kinematic range $2 < p_T < 20$ GeV/c and $1.5 < y < 3.5$ for the pPb configuration, and in the range $2 < p_T < 20$ GeV/c and $-4.5 < y < -2.5$ for the Pbp configuration. The p_T intervals used to study the efficiency and signal yield are 2–4 GeV/c, 4–7 GeV/c, 7–12 GeV/c and 12–20 GeV/c, and the rapidity regions are split into two equal size intervals, $-4.5 < y < -3.5$ and $-3.5 < y < -2.5$ for the pPb configuration, and $1.5 < y < 2.5$ and $2.5 < y < 3.5$ for the Pbp configuration. The range $p_T < 2$ GeV/c is not considered due to the small signal yield with the current sample. This restriction is not related to any detector limitation specific to the collision system, but to the limited integrated luminosity and the small production cross section.

Nuclear effects are quantified by the nuclear modification factor, $R_{p\text{Pb}}$,

$$R_{p\text{Pb}}(p_T, y) \equiv \frac{1}{A_{\text{Pb}}} \frac{d^2\sigma_{p\text{Pb}}(p_T, y)/dp_T dy}{d^2\sigma_{pp}(p_T, y)/dp_T dy}, \qquad (2)$$

where $A_{\text{Pb}} = 208$ is the mass number of the lead ion, $d^2\sigma_{p\text{Pb}}(p_T, y)/dp_T dy$ the H_b production cross section in proton-lead collisions as defined in Eq. (1), and $d^2\sigma_{pp}(p_T, y)/dp_T dy$ the H_b reference production cross section in pp collisions at the same nucleon-nucleon center-of-mass energy. In the absence of nuclear effects, the nuclear modification factor is equal to unity.

To quantify the relative forward-to-backward production rates, the forward-to-backward ratio, R_{FB}, is measured, which is the ratio of cross sections in the positive and negative y intervals corresponding to the same absolute value range,

$$R_{\text{FB}}(p_T, y) \equiv \frac{d^2\sigma_{p\text{Pb}}(p_T, +|y|)/dp_T dy}{d^2\sigma_{p\text{Pb}}(p_T, -|y|)/dp_T dy}. \qquad (3)$$

III. SELECTIONS, SIGNAL YIELDS AND EFFICIENCY

A. Candidate reconstruction and selection

The B^+ cross section is measured in the $B^+ \to J/\psi K^+$ mode, with $J/\psi \to \mu^+\mu^-$, and in the purely hadronic mode

$B^+ \to \bar{D}^0\pi^+$, with $\bar{D}^0 \to K^+\pi^-$. The cross sections of the B^0 and Λ_b^0 hadrons are studied in the hadronic decays $B^0 \to D^-\pi^+$ with $D^- \to K^+\pi^-\pi^-$ and $\Lambda_b^0 \to \Lambda_c^+\pi^-$ with $\Lambda_c^+ \to pK^-\pi^+$.

For the $B^+ \to \bar{D}^0\pi^+$, $B^0 \to D^-\pi^+$ and $\Lambda_b^0 \to \Lambda_c^+\pi^-$ hadronic modes, the candidates are reconstructed from a sample selected by a hardware trigger requiring a minimum activity in the scintillating-pad detector. This hardware trigger selection has an efficiency of 100% for the signal. The intermediate charm-hadron candidates are reconstructed using tracks that are identified as pion, kaon and proton candidates by the LHCb particle identification system [27]. The tracks used to form the $\bar{D}^0$ (D^- and Λ_c^+) candidates are required to have $p_T > 300$ MeV/c, and at least one of them has to satisfy $p_T > 500$ MeV/c ($p_T > 1000$ MeV/c). They must also have momentum $p > 3$ GeV/c ($p > 10$ GeV/c for protons) and pseudorapidity in the range $2 < \eta < 5$. In addition, they are required to be separated from any primary vertex by requiring $\chi_{\text{IP}}^2 > 16$, where χ_{IP}^2 is the difference between the χ^2 values of a given PV reconstructed with and without the considered track. The tracks are required to form a vertex of good quality. Further requirements are imposed to ensure that this vertex is consistent with charm-hadron decays by requiring a minimum reconstructed decay time and a reconstructed mass within an interval centered on the known values of the hadron mass [43]: [1834.8, 1894.8] MeV/c^2, [1844.6, 1894.6] MeV/c^2 and [2268.5, 2304.5] MeV/c^2 for $\bar{D}^0$, D^- and Λ_c^+ candidates, respectively. Each mass interval corresponds to six times the experimental resolution on the reconstructed mass. A charm-hadron candidate, inconsistent with originating from the PVs as ensured by the requirement $\chi_{\text{IP}}^2 > 4$, is then combined with a positively identified pion of the appropriate charge to form a beauty hadron. This pion is required to have $p_T > 500$ MeV/c and to be separated from any PV with the condition $\chi_{\text{IP}}^2 > 16$. Reconstructed beauty hadrons with a good-quality vertex and a significant displacement from any PV are selected and are further required to point back to a PV by imposing $\chi_{\text{IP}}^2 < 16$. The offline selected beauty-hadron candidates are also required to match an online vertex, reconstructed from two, three or four tracks, with a large sum of the transverse momenta of the tracks and a significant displacement from the PVs.

The B^+ candidates studied with the $B^+ \to J/\psi K^+$ decay are obtained from a data sample that contains J/ψ candidates reconstructed by the online software trigger [34]. The muons used to reconstruct a J/ψ meson are identified by the muon detector and information from all subsystems combined by a neural network. The J/ψ candidate must have a well-reconstructed vertex, a mass in the range [3056.9, 3136.9] MeV/c^2, and pass the hardware trigger that selects muons with $p_T > 500$ MeV/c. The J/ψ candidate with a reconstructed decay vertex

significantly separated from all PVs is combined with a kaon track to form a B^+ candidate. The K^+ candidate must be positively identified and is required to have a transverse momentum $p_T > 500$ MeV/c and to be separated from all PVs with the requirement $\chi^2_{IP} > 16$. The reconstructed B^+ candidate is required to have a good-quality vertex, be displaced from the PVs and point back to a PV by requiring $\chi^2_{IP} < 16$.

B. Signal yield determination

The signal yields for each decay mode are determined from extended unbinned maximum-likelihood fits to their mass distributions. The fits are used to calculate per-candidate weights with the *sPlot* method [44]. The weights are then used to determine the signal yields in each p_T and y bin. As a cross-check, fits are also performed in individual p_T and y bins, and the results are consistent with those obtained using the *sPlot* method.

The signal mass distribution is described by a Crystal Ball (CB) function [45] for the $B^+ \rightarrow J/\psi K^+$, $B^0 \rightarrow D^- \pi^+$ and $\Lambda_b^0 \rightarrow \Lambda_c^+ \pi^-$ decays. For the $B^+ \rightarrow \bar{D}^0 \pi^+$ decay an additional Gaussian function, which shares the peak position with the CB function, is necessary to achieve a satisfactory fit quality. The tail parameters for the CB function and the fractions of the CB and the Gaussian components are fixed to values obtained from fits to mass spectra of simulated signal decays. The mean and width of the Gaussian core in the CB function, and the width of the separate Gaussian component are free parameters determined from data. The combinatorial background is described by an exponential function, with parameters allowed to vary in the fits.

The contribution of misidentified background from $B^+ \rightarrow \bar{D}^0 K^+$, $B^0 \rightarrow D^- K^+$ and $\Lambda_b^0 \rightarrow \Lambda_c^+ K^-$ ($B^+ \rightarrow J/\psi \pi^+$) decays, where the $K^{\pm}$ (π^+) meson is reconstructed as a $\pi^{\pm}$ (K^+) candidate, is described by an empirical function obtained using simulation. Due to the small branching fraction of the misidentified background compared to the signal and the suppression from the PID requirement, the contribution relative to the signal mode in the selected sample is expected to be around or below 5% depending on the decay mode.

For the $B^+ \rightarrow \bar{D}^0 \pi^+$ decay, the partially reconstructed backgrounds of $B^{0,+} \rightarrow \bar{D}^{*-,0} \pi^+$ with $\bar{D}^{*0} \rightarrow \bar{D}^0 \gamma$ or $\bar{D}^{*-,0} \rightarrow \bar{D}^0 \pi^{-,0}$, and $B^{0,+} \rightarrow \bar{D}^0 \rho^{0,+}$ decays with $\rho^{0,+} \rightarrow \pi^+ \pi^{-,0}$, where only the $\bar{D}^0 \pi^+$ in the final states are reconstructed, are modeled with polynomials convolved with a Gaussian resolution function, following the method described in Ref. [46]. The partially reconstructed backgrounds of $B^{-,0} \rightarrow D^- \rho^{0,+}$ and $\Lambda_b^0 \rightarrow \Lambda_c^+ \rho^-$ ($B^{0,+} \rightarrow J/\psi K^{*0,+}$) decays, with $\rho^{0,\pm} \rightarrow \pi^{\pm} \pi^{\mp,0}$ ($K^{*0,+} \rightarrow K^+ \pi^{-,0}$), in the $B^0 \rightarrow D^- \pi^+$ and $\Lambda_b^0 \rightarrow \Lambda_c^+ \pi^-$ ($B^+ \rightarrow J/\psi K^+$) mass distributions are described by a threshold function [47] convolved with a Gaussian function to account for

resolution effects. The resolution function is the same as that of the Gaussian kernel for the signal component.

The shape for each component, except that of the combinatorial background, is constrained to be the same for the fits to pPb and Pbp data. The yields for each contribution in the fit model are free parameters determined from data with the constraint that the ratio of misidentified background to signal yield is the same in pPb and Pbp data. The signal yields for each decay model considered in this analysis are summarized in Table I for the kinematic range $2 < p_T < 20$ GeV/c and $1.5 < y < 3.5$ $(-4.5 < y < -2.5)$ in the pPb (Pbp) sample. The mass distributions and the fit projections are shown in Figs. 1–4 for the decays $B^+ \rightarrow \bar{D}^0 \pi^+$, $B^+ \rightarrow J/\psi K^+$, $B^0 \rightarrow D^- \pi^+$ and $\Lambda_b^0 \rightarrow \Lambda_c^+ \pi^-$, respectively. The higher combinatorial background level in the Pbp sample compared to the pPb sample is due to higher charged track multiplicities seen by the LHCb detector in the Pbp beam configuration.

C. Efficiency

The total efficiency is the product of the geometrical acceptance of the detector and the efficiencies of the reconstruction, the selection, the PID and the trigger requirements. It is about a few percent in the low-p_T region, and 20% in the high-p_T region. These efficiencies, except for the PID, are evaluated using samples of simulated signal decays, in bins of the beauty-hadron p_T and y. The reconstruction efficiency obtained from simulated signals is corrected using a data-driven method which is detailed in the next paragraph. The occupancy distribution in the minimum bias simulation sample is weighted to reproduce that in data, in order to model correctly the PV reconstruction efficiency. For the decays $B^+ \rightarrow \bar{D}^0 \pi^+$, $B^+ \rightarrow J/\psi K^+$ and $B^0 \rightarrow D^- \pi^+$ and subsequent charm-hadron decays, the angular distributions of the final state particles are well described by EvtGen. For the $\Lambda_b^0 \rightarrow \Lambda_c^+ \pi^-$ decay, the Dalitz-plot distribution of the $\Lambda_c^+ \rightarrow p K^- \pi^+$ decay in simulation is described by a mixture of uniform phase space and resonant contributions of $\Delta(1232)^{++} \rightarrow p \pi^+$ and $K^*(892)^0 \rightarrow K^- \pi^+$. The Λ_c^+ Dalitz-plot distribution in the simulation is corrected to match that in the background subtracted data.

The track reconstruction efficiency from simulation is corrected using a tag-and-probe approach. For this method,

TABLE I. Signal yields in the range $2 < p_T < 20$ GeV/c and $1.5 < y < 3.5$ $(-4.5 < y < -2.5)$ for pPb (Pbp) collisions. Uncertainties are statistical only.

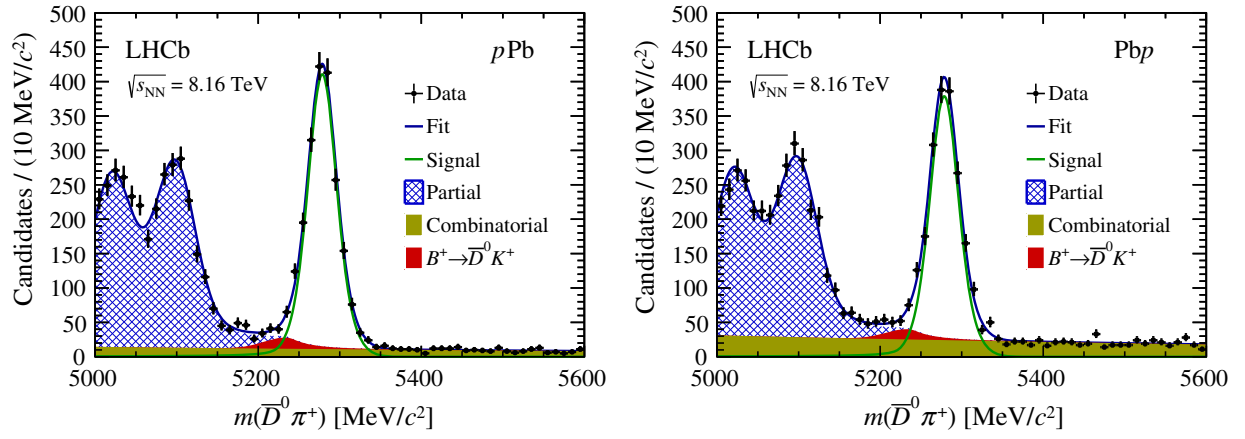| Decay	pPb	Pbp
$B^+ \rightarrow \bar{D}^0 \pi^+$	1958 ± 54	1806 ± 55
$B^+ \rightarrow J/\psi K^+$	0883 ± 32	0907 ± 33
$B^0 \rightarrow D^- \pi^+$	1151 ± 38	0889 ± 34
$\Lambda_b^0 \rightarrow \Lambda_c^+ \pi^-$	0484 ± 24	0399 ± 23

FIG. 1. Invariant mass distribution of B^+ candidates reconstructed in the $B^+ \to \bar{D}^0 \pi^+$ decay for (left) pPb and (right) Pbp collisions, with the fit result superimposed. The solid blue line, the solid green line, the cross-shaded area, the brown shaded area and the red shaded area represent the total fit, the signal component, the partially reconstructed background, the combinatorial background and $B^+ \to \bar{D}^0 K^+$ decays, respectively.
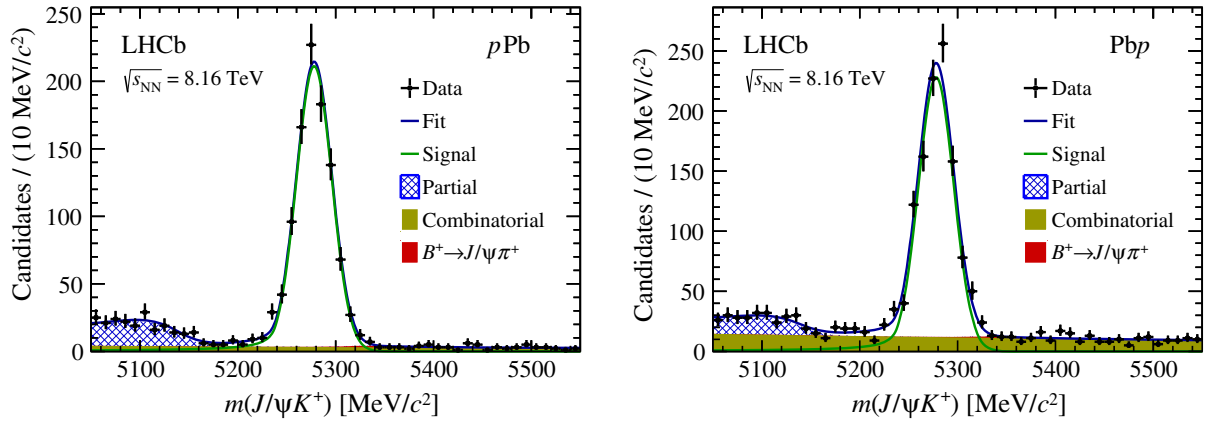
FIG. 2. Invariant mass distribution of B^+ candidates reconstructed in the $B^+ \to J/\psi K^+$ decay for (left) pPb and (right) Pbp collisions, with the fit result superimposed. The solid blue line, the solid green line, the cross-shaded area, the brown shaded area and the red shaded area represent the total fit, the signal component, the partially reconstructed background, the combinatorial background and $B^+ \to J/\psi \pi^+$ decays, respectively.
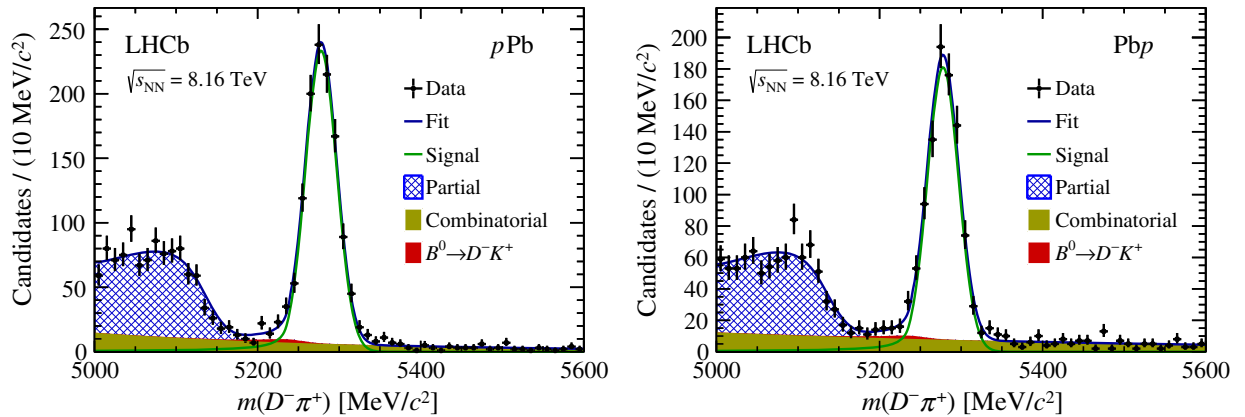
FIG. 3. Invariant mass distribution of B^0 candidates reconstructed in the $B^0 \to D^- \pi^+$ decay for (left) pPb and (right) Pbp collisions, with the fit result superimposed. The solid blue line, the solid green line, the cross-shaded area, the brown shaded area and the red shaded area represent the total fit, the signal component, the partially reconstructed background, the combinatorial background and $B^0 \to D^- K^+$ decays, respectively.

FIG. 4.   Invariant mass distribution of Λ_b^0 candidates reconstructed in the $\Lambda_b^0 \to \Lambda_c^+ \pi^-$ decay for (left) pPb and (right) Pbp collisions, with the fit result superimposed. The solid blue line, the solid green line, the cross-shaded area, the brown shaded area and the red shaded area represent the total fit, the signal component, the partially reconstructed background, the combinatorial background and $\Lambda_b^0 \to \Lambda_c^+ K^-$ decays, respectively.
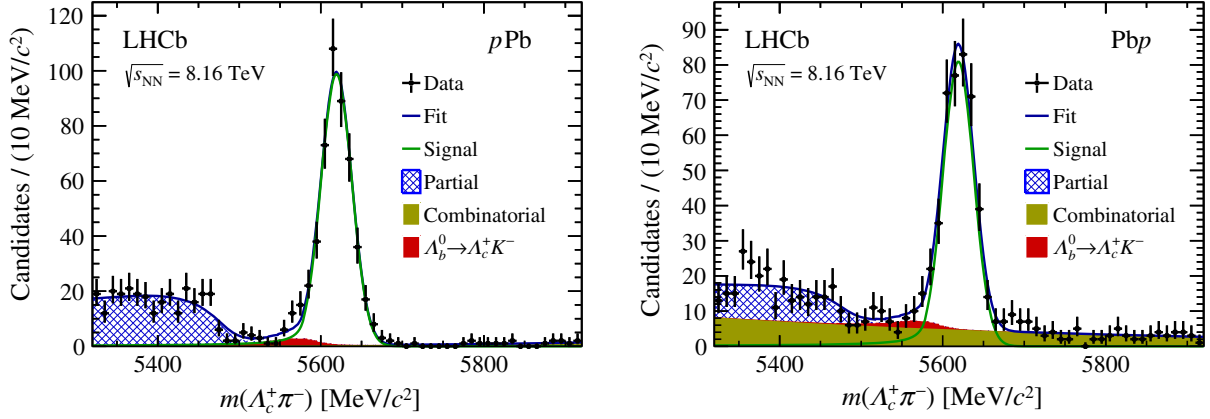
J/ψ candidates in data are formed combining a fully reconstructed "tag" track with a "probe" track reconstructed using a subset of the tracking detectors [27,48]. The single-track reconstruction efficiency is obtained as the fraction of the probe tracks that are matched to fully reconstructed tracks, in bins of the track momentum and pseudorapidity. The ratio of the tag-and-probe efficiency between proton-lead data and simulation is used to correct the simulation efficiencies. The correction factors are determined for the pPb and Pbp samples separately.

The PID efficiency for each track is determined with a tag-and-probe method [49,50] using calibration samples of proton-lead data. The track PID efficiency depends on the detector occupancy. Since the occupancy distribution is found to be consistent between the calibration samples and the beauty-signal events, the efficiency is parametrized as a function of track momentum and pseudorapidity. The pion

and kaon PID efficiencies are calibrated using $D^0 \to K^- \pi^+$ decays, where the D^0 flavor is tagged by the charge of the pion in $D^{*+} \to D^0 \pi^+$ decays, the proton PID efficiency is studied using $\Lambda \to p\pi^-$ decays and the PID efficiency for muons is obtained using $J/\psi \to \mu^+ \mu^-$ decays. For each beauty candidate, the product of the single-track PID efficiencies, measured as a function of the track momenta and pseudorapidity, gives the combined PID efficiency for all the tracks in the final state. The efficiency is then averaged over all beauty-hadron candidates for each bin of p_T and y.

IV. SYSTEMATIC UNCERTAINTIES

The various sources of systematic uncertainties, and their quadratic sum, on the cross sections for B^+, B^0 and Λ_b^0 hadrons are summarized in Tables II and III for the pPb and

TABLE II.   Summary of systematic uncertainties (in %) for the measured cross sections for different decay modes in pPb. The ranges correspond to the minimum and maximum values over the p_T and y bins of the measurement.

Source	$B^+ \to J/\psi K^+$	$B^+ \to \bar{D}^0 \pi^+$	$B^0 \to D^- \pi^+$	$\Lambda_b^0 \to \Lambda_c^+ \pi^-$
Luminosity	2.6	2.6	2.6	2.6
Trigger	1.0	1.0	1.0	1.0
Signal yield	2.0	2.0	2.0	2.0
Selection	1.0	1.0	3.0	2.0
Hadron tracking	1.5	4.5	6.0	6.0
Tracking efficiency method	2.4	2.4	3.2	3.2
Tracking sample size	2.0–4.3	2.4–4.9	3.4–9.5	3.3–8.0
Branching fraction	3.1	3.2	6.0	9.6
PID binning	0.0–0.7	0.0–0.6	0.0–0.9	0.1–1.4
PID sample size	1.4–2.7	0.2–0.6	0.2–0.7	0.2–0.4
Kinematics	0.1–4.1	0.5–5.4	0.1–7.0	0.2–9.4
Dalitz structure	–	–	–	0.8–3.1
Simulation sample size	0.7–2.2	0.8–2.4	1.4–3.7	0.9–4.1
Total	6.3–8.1	7.5–10.3	10.9–14.5	13.1–18.3

TABLE III.   Summary of systematic uncertainties (in %) for the measured cross sections for different decay modes in Pbp. The ranges correspond to the minimum and maximum values over the p_{T} and y bins of the measurement.

Source	$B^+ \to J/\psi K^+$	$B^+ \to \bar{D}^0 \pi^+$	$B^0 \to D^- \pi^+$	$\Lambda_b^0 \to \Lambda_c^+ \pi^-$
Luminosity	2.5	2.5	2.5	2.5
Trigger	1.0	1.0	1.0	1.0
Signal yield	2.0	2.0	2.0	2.0
Selection	1.0	1.0	3.0	2.0
Hadron tracking	1.5	4.5	6.0	6.0
Tracking efficiency method	2.4	2.4	3.2	3.2
Tracking sample size	4.6–11.1	5.4–10.5	7.8–17.8	7.7–14.7
Branching fraction	3.1	3.2	6.0	9.6
PID binning	0.0–1.0	0.1–0.7	0.0–0.6	0.1–1.4
PID sample size	0.7–2.1	0.1–0.4	0.2–0.5	0.1–0.2
Kinematics	0.7–3.9	0.1–2.5	0.5–1.9	0.3–6.9
Dalitz structure	–	–	–	0.8–3.1
Simulation sample size	0.8–2.6	1.1–2.7	1.9–3.8	1.9–3.9
Total	7.4–12.7	9.0–13.1	13.0–20.9	15.1–21.3

Pbp data samples, respectively. The ranges in the tables correspond to the minimum and maximum values over the p_{T} and y bins of the measurement. The cross section of the B^+ hadron is measured in the two decay modes, $B^+ \to J/\psi K^+$ and $B^+ \to \bar{D}^0 \pi^+$, which give consistent results within statistical uncertainties.

The uncertainty on the b-hadron signal yields is studied by using alternative fit models or different fitting ranges for the mass distributions. The nominal CB function for the signal mass distribution is replaced by a combination of a Gaussian function plus a CB function or vice versa for the $B^+ \to \bar{D}^0 \pi^+$ decay, giving a relative change of 2% on the signal yields for all the decay modes. A second-order polynomial is employed to replace the exponential function for the combinatorial background, which results in a difference of 1% for the signal yields at the maximum. The effect of partially reconstructed background is studied by fitting the mass distribution in a smaller region where its contribution is reduced or absent. The signal yields change by at most 1% for all the decay channels. The effect of the misidentified background is studied by fixing its branching fraction relative to that of the signal [43], corrected by the PID selection efficiency. The change in signal yields amounts to 0.1%. The maximum value among all these effects, 2%, is quoted as the systematic uncertainty, and is considered as a global uncertainty for all decay modes and all p_{T} and y bins.

The corrections to the track reconstruction efficiency are limited in precision by the size of the calibration data sample, which results in a systematic uncertainty dominating in most of the analysis bins. This effect is studied by generating sets of correction factors according to Gaussian distributions centered on their nominal values and with widths equal to the statistical uncertainties. The standard deviation of the variations of the corrected efficiency in simulation is assigned as uncertainty, labeled as "tracking

sample size" in the summary tables. It ranges from 2.0% to 9.5% for pPb and from 4.6% to 17.8% for Pbp, depending on the decay modes and the beauty-hadron p_{T} and y bins. The larger uncertainty for the Pbp sample, where the LHCb detector accepts particles produced in the lead beam direction, is due to higher background that makes the signal yield determination in the calibration data sample more difficult. The tag-and-probe method used to calculate the tracking efficiency has an uncertainty estimated to be 0.8% per track [48], giving a total value of 2.4% (3.2%) for a three- (four-)track decay mode. Since the tracking efficiency is measured using muons, an additional uncertainty of 1.5% per track is introduced for hadrons, to account for the possible imperfect modeling of the amount of interactions with the detector material. Labeled as "hadron tracking" in the summary tables, the result is equal to 1.5% for $B^+ \to J/\psi K^+$ and to 4.5% (6%) for three- (four-)track hadronic decays. The uncertainties related to the track reconstruction efficiency method and to the hadron-detector interactions are fully correlated among different hadron species and between the pPb, Pbp and pp datasets.

Several sources of systematic uncertainties are associated with the PID efficiencies. The contribution due to the limited size of the data calibration samples is determined by varying the single-track PID efficiencies within their uncertainties for all momentum and pseudorapidity bins simultaneously, and calculating the resulting spread of the PID efficiencies on the b-hadron signal decays. Since large samples are available for the kaon, pion, and proton calibration, the resulting systematic uncertainties are found to be small and in the range of 0.2%–0.7% (0.1%–0.5%) for the $B^+ \to \bar{D}^0 \pi^+$ decay, $B^0 \to D^- \pi^+$ and $\Lambda_b^0 \to \Lambda_c^+ \pi^-$ decays in pPb (Pbp) collisions. They are labeled as "PID sample size" in the summary tables. For $B^+ \to J/\psi K^+$ decays, the smaller size of the muon calibration

samples results in a systematic uncertainty between 1.4% and 2.7% for the pPb data and between 0.7% and 2.1% for the Pbp data. For each bin of track momentum and pseudorapidity, the possible difference in track kinematics between the PID sample and the b-hadron sample is counted as a second source of systematic uncertainty. The effect is studied by varying the default binning scheme using finer bins, and determining the changes of the PID efficiencies on the b-hadron signal decays. The result is labelled as "PID binning" in the summary tables and is found to be at most 1.4%. The systematic uncertainty related to a possible difference of detector occupancy between the PID samples and the b-hadron samples is studied by weighting the occupancy in the PID samples to match that of the signal beauty sample, and the resulting change of the efficiency is found to be negligible.

The imperfect modeling of b-hadron kinematic distributions and decay properties in the simulation introduces systematic uncertainties on the reconstruction and selection efficiencies. The two-body invariant mass distributions of the Λ_c^+ decay products, or Dalitz-plot distribution, for the $\Lambda_b^0 \to \Lambda_c^+ \pi^-$ mode in simulation is weighted to match data, and the uncertainty on the Dalitz-plot distribution is counted as a source of systematic uncertainty. Its magnitude is studied by pseudoexperiments. For each pseudoexperiment, a sample is constructed by randomly sampling Λ_b^0 candidates from data allowing for repetition, and this sample is used to correct the Dalitz-plot distribution in the simulation. The root-mean-square value of the efficiencies corrected with multiple pseudoexperiments is quoted as the systematic uncertainty. It is found to be in the range 0.8%–3.1% for the different Λ_b^0 p_T and y bins and is labeled as "Dalitz structure" in the summary tables.

The distributions of variables used to select candidates show good agreement between data and simulation. The effect of the residual differences is quantified by weighting the reconstructed b-hadron decay-time distribution in simulation to match that in data, and studying the corresponding variation of the selection efficiency. The result, labeled as "selection" in the summary tables, amounts to 1% for the two B^+ decay modes, and to 3% and 2% for the B^0 and Λ_b^0 decay modes.

Simulation and data also show reasonable agreement in the beauty-hadron p_T and y distribution, even if a modest discrepancy in the p_T distribution is observed, especially for the Λ_b^0 baryon. Due to the limited data sample size it is not possible to accurately determine the b-hadron p_T and y distributions from data directly. However, as the cross section is measured differentially in bins of p_T and y, the small discrepancy on these kinematic distributions has a reduced impact. A systematic uncertainty is evaluated as the change in the reconstruction efficiency after reweighting the p_T and y distributions in simulation to match data using a finer binning scheme. The result, labeled as "kinematics" in the summary tables, ranges from a fraction of a percent to a few percent depending on the decay modes and the beauty-hadron p_T and y bins.

The muon trigger efficiency is validated using a large sample of $J/\psi \to \mu^+ \mu^-$ decays obtained with an unbiased trigger selection [32]. The result is compared with the trigger efficiency estimated in simulation, showing a difference of at most 1%, which is quoted as the systematic uncertainty due to the trigger selection for the $B^+ \to J/\psi K^+$ decay. Thanks to the loose requirement applied by the online event selection, the overall trigger efficiency for the purely hadronic decay modes is found to be above 99% for the offline selected candidates. A systematic uncertainty of 1% is assigned.

The finite sizes of the simulated b-hadron signal samples introduce uncertainties on the efficiency, which are propagated to the cross section. Labeled as "simulation sample size," these uncertainties range from subpercent to a few percent depending on the decay modes and the p_T and y bins. The uncertainties due to the integrated luminosity of the pPb and Pbp datasets are of 2.6% and 2.5%, respectively. The uncertainties on the branching fractions of the b-hadron decays and of the intermediate charm-hadron decays are also sources of systematic uncertainty, and are evaluated using the uncertainties on the measured values [43].

The dominant systematic effect is the uncertainty on the track reconstruction efficiency which, however, largely cancels in the cross section ratios. For the $\Lambda_b^0 \to \Lambda_c^+ \pi^-$ decay, the branching fraction is also a large source of systematic uncertainty, but cancels for the nuclear modification factor measurements. The systematic uncertainties are considered to be fully correlated among all kinematic bins for a particular decay mode, except that labeled as "simulation sample size" which is uncorrelated.

V. RESULTS

A. Cross sections

The B^+ cross sections measured in the $J/\psi K^+$ and $\bar{D}^0 \pi^+$ decay modes are consistent and their weighted average is reported. The weights are calculated using the statistical uncertainties combined with the systematic uncertainty due to the limited sample size of the simulation samples. The systematic uncertainties due to luminosity, kinematics, track reconstruction efficiency and kaon PID efficiency are entirely or strongly correlated, while those due to simulation sample size, muon and pion PID efficiencies, trigger selection and branching fractions are uncorrelated between the two decay modes. The double-differential cross section of the averaged B^+ production in four rapidity bins as a function of p_T and integrated over p_T as a function of rapidity are shown in Fig. 5 and reported in Table IV. The same quantities for B^0 production are displayed in Fig. 6 and listed in Table IV. The measured cross sections increase toward central rapidity both at positive and at negative
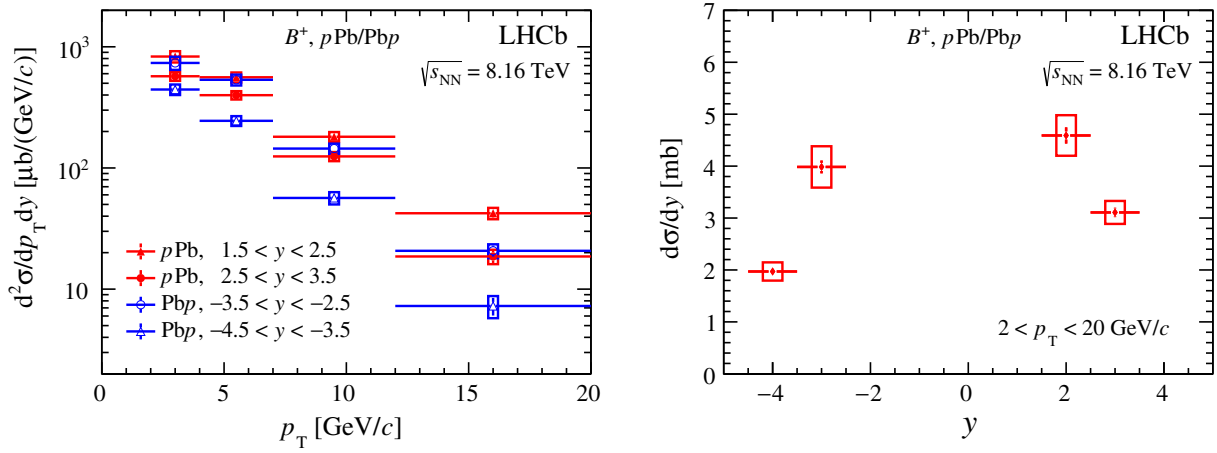
FIG. 5. Production cross section of B^+ mesons as a function of (left) p_T in y bins and (right) y integrated over p_T. The vertical bars (boxes) show statistical (total) uncertainties.

rapidity. A good precision is achieved in the B^+ sample due to the averaging over two decay channels, which allows for improved precision with respect to the measurement in each single B^+ decay mode.

The double-differential cross section of Λ_b^0 production is shown in Fig. 7 in four rapidity bins as a function of p_T and integrated over p_T as a function of rapidity, and is listed in Table IV. The trend observed as a function of the two variables is similar to that of the B mesons.

In order to probe the hadronization in proton-lead collisions, ratios of B^0 over B^+ and Λ_b^0 over B^0 production cross sections are studied with results shown in Fig. 8.

Both ratios show no significant rapidity dependence within experimental uncertainties. The ratio between meson species is consistent with being independent of y and p_T of the beauty hadrons. Most interestingly, the baryon-to-meson ratio shows a p_T dependence with a significantly lower value at the highest p_T compared to the p_T-integrated measurement. However, the current uncertainties do not allow us to draw firm conclusions. The production ratio, averaged over the kinematic range in the analysis, is measured to be 0.41 ± 0.06 (0.39 ± 0.05) for the pPb (Pbp) sample. The value is consistent with that measured by the LHCb collaboration in pp collisions [22–25].

TABLE IV. Differential cross sections of B^+, B^0 and Λ_b^0 production in bins of p_T and y, $\frac{d^2\sigma}{dp_T dy}$ (μb/[GeV/c]), and in bins of y integrated over $2 < p_T < 20$ GeV/c, $\frac{d\sigma}{dy}$ (μb). The first uncertainty is statistical and the second systematic.

| p_T (GeV/c)	$-4.5 < y < -3.5$	$-3.5 < y < -2.5$	$1.5 < y < 2.5$	$2.5 < y < 3.5$
		B^+		
(2, 4)	$441.1 \pm 25.8 \pm 36.0$	$735.7 \pm 45.6 \pm 78.7$	$831.1 \pm 54.8 \pm 69.8$	$571.3 \pm 30.8 \pm 36.6$
(4, 7)	$244.9 \pm 12.5 \pm 19.1$	$534.2 \pm 24.6 \pm 49.1$	$560.3 \pm 30.8 \pm 43.7$	$398.7 \pm 17.9 \pm 25.9$
(7, 12)	$56.6 \pm 4.2 \pm 5.0$	$144.5 \pm 8.1 \pm 11.7$	$181.0 \pm 10.5 \pm 13.2$	$124.5 \pm 7.0 \pm 8.2$
(12, 20)	$7.3 \pm 1.2 \pm 0.9$	$20.7 \pm 2.1 \pm 1.7$	$42.3 \pm 3.5 \pm 3.0$	$18.6 \pm 2.2 \pm 1.3$
(2, 20)	$1971 \pm 69 \pm 162$	$3984 \pm 124 \pm 378$	$4590 \pm 156 \pm 358$	$3108 \pm 90 \pm 202$
		B^0		
(2, 4)	$396.2 \pm 56.7 \pm 63.8$	$1020.8 \pm 136.8 \pm 213.3$	$898.0 \pm 144.6 \pm 130.2$	$645.9 \pm 70.4 \pm 81.4$
(4, 7)	$301.3 \pm 25.6 \pm 41.0$	$578.2 \pm 50.9 \pm 100.6$	$676.6 \pm 62.2 \pm 88.6$	$453.6 \pm 32.2 \pm 50.8$
(7, 12)	$66.8 \pm 6.6 \pm 8.7$	$175.7 \pm 14.2 \pm 26.0$	$237.8 \pm 19.7 \pm 29.7$	$154.8 \pm 11.1 \pm 16.9$
(12, 20)	$7.1 \pm 1.6 \pm 1.0$	$30.8 \pm 3.7 \pm 4.3$	$37.5 \pm 4.4 \pm 4.4$	$29.0 \pm 3.3 \pm 3.2$
(2, 20)	$2086 \pm 142 \pm 298$	$4890 \pm 323 \pm 875$	$5332 \pm 357 \pm 693$	$3658 \pm 183 \pm 417$
		Λ_b^0		
(2, 4)	$196.3 \pm 35.7 \pm 33.4$	$242.1 \pm 84.0 \pm 51.1$	$441.2 \pm 102.4 \pm 80.7$	$276.1 \pm 43.6 \pm 39.5$
(4, 7)	$106.8 \pm 14.9 \pm 16.8$	$244.6 \pm 33.7 \pm 43.3$	$289.5 \pm 40.8 \pm 44.6$	$219.7 \pm 21.1 \pm 29.0$
(7, 12)	$35.7 \pm 4.4 \pm 5.4$	$85.6 \pm 9.2 \pm 13.6$	$107.5 \pm 11.9 \pm 14.7$	$48.7 \pm 5.7 \pm 6.4$
(12, 20)	$1.6 \pm 0.6 \pm 0.2$	$6.7 \pm 1.4 \pm 1.1$	$8.3 \pm 1.9 \pm 1.1$	$5.9 \pm 1.4 \pm 0.8$
(2, 20)	$935 \pm 91 \pm 149$	$1658 \pm 194 \pm 293$	$2305 \pm 244 \pm 360$	$1480 \pm 111 \pm 198$
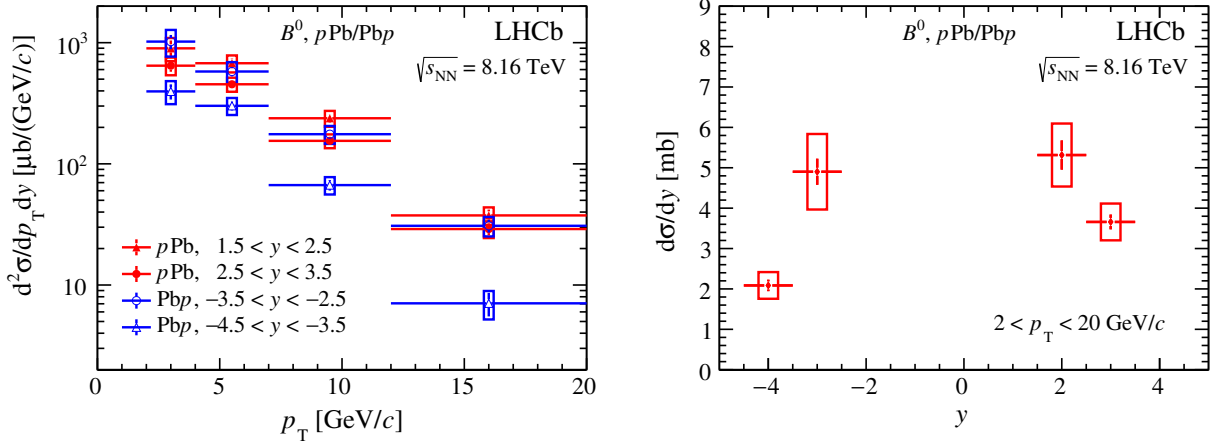
FIG. 6.   Production cross section of B^0 mesons as function of (left) p_T in y bins and (right) y integrated over p_T. The vertical bars (boxes) show statistical (total) uncertainties.

FIG. 7.   Production cross section of Λ_b^0 baryons as a function of (left) p_T in y bins and (right) y integrated over p_T. The vertical bars (boxes) show statistical (total) uncertainties.
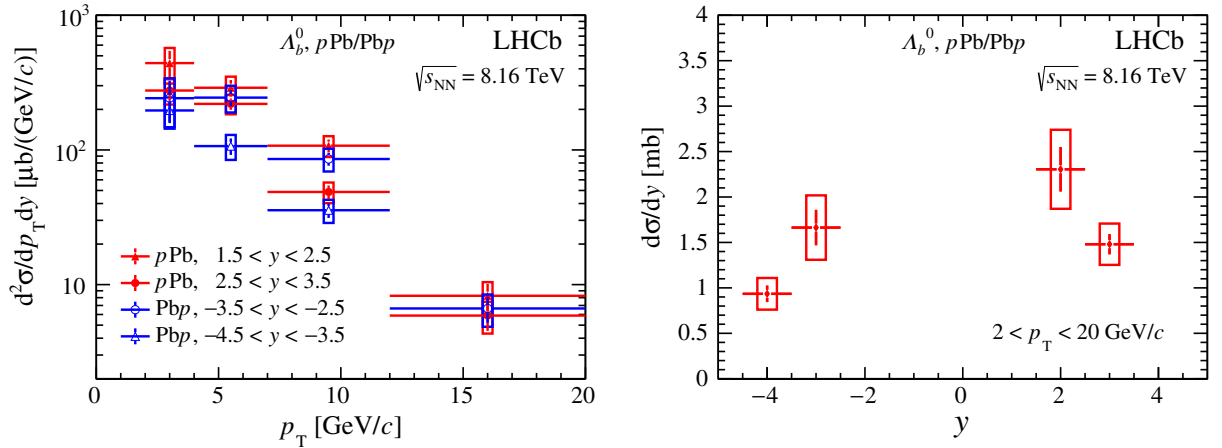
The cross sections are used to calculate forward-backward ratios and nuclear modification factors. In the following, the experimental results on these nuclear modification observables are compared with calculations using the HELAC-onia generator [51–53] with two different nuclear parton distribution function (nPDF) sets, nCTEQ15 [6] and EPPS16 [7]. For these calculations, the model parameters are tuned to reproduce pp cross section measurements at the LHC. The uncertainties reflect those from the corresponding nPDF parametrizations, and correspond to a 68% confidence interval. A weighting of the current nPDF sets with heavy-flavor measurements at the LHC was performed [19] under the assumption that the modification of the nPDF is the main mechanism of nuclear modification of heavy-flavor production. The corresponding predictions are shown together with their uncertainty bands under the label EPPS16∗ [19]. In the HELAC-onia framework, the nuclear matter effects are similar for the B^+,

B^0 and Λ_b^0 hadrons, i.e., those possibly affecting the b-quark hadronization are not included. For this reason, in the following the predictions are only compared with B^+ production.

B. Forward-backward ratios

The forward-backward production ratio of B^+ mesons is shown in Fig. 9 as a function of p_T and y, while the corresponding values are reported in Table V. A significant suppression of the production in the pPb sample with respect to that in the Pbp data is measured at the level of 20% when integrating over p_T. Within the experimental uncertainty, no dependence as a function of p_T is observed. The HELAC-onia calculations using EPPS16 and nCTEQ15 are in agreement with the experimental data. The EPPS16∗ set exhibits the smallest uncertainties and is also in agreement with data.
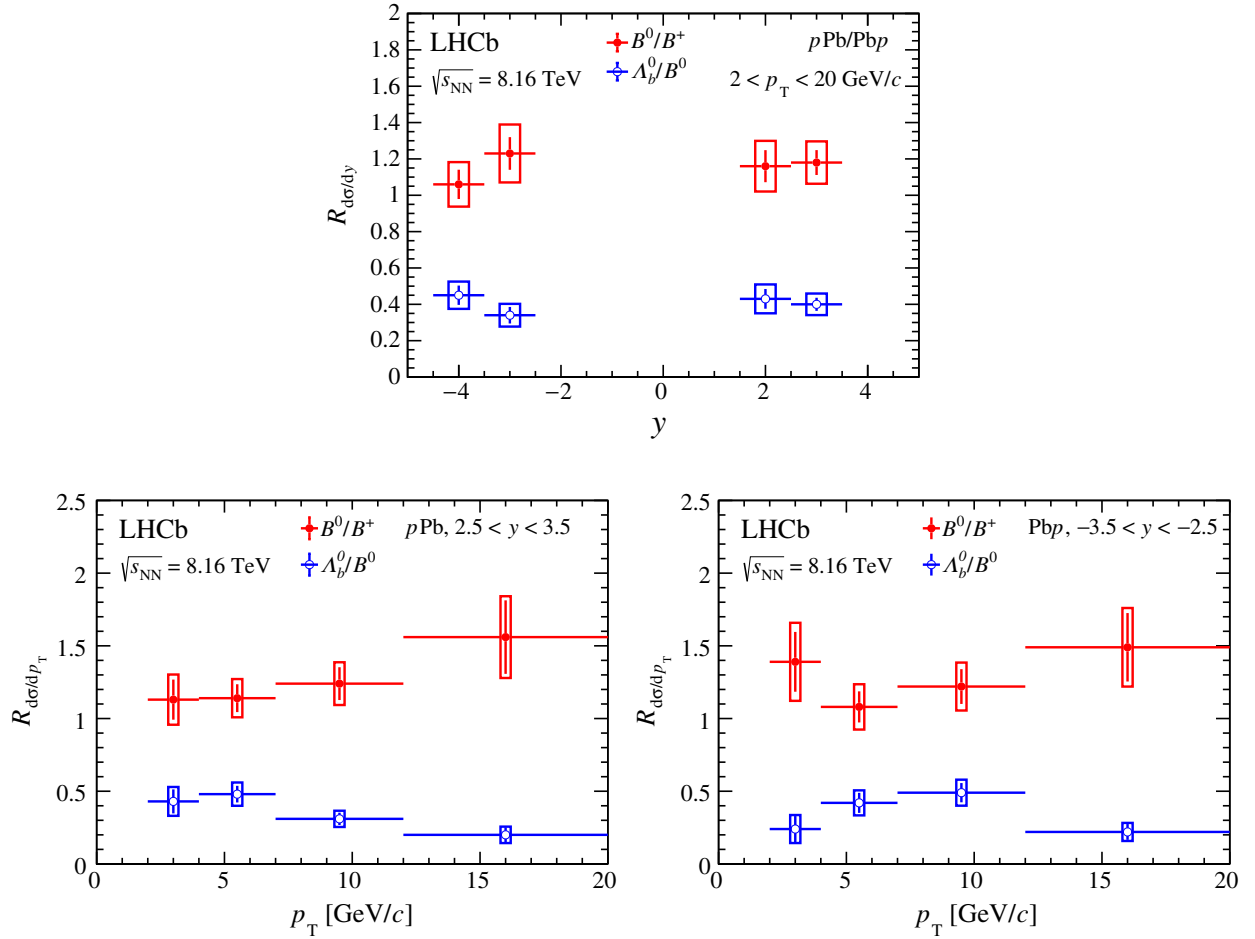
FIG. 8. Production cross section ratios of Λ_b^0 baryons over B^0 mesons and of B^0 mesons over B^+ mesons (top) as a function of y integrated over p_T and as a function of p_T for (bottom left) $2.5 < y < 3.5$ and (bottom right) $-3.5 < y < -2.5$. The vertical bars (boxes) show statistical (total) uncertainties.
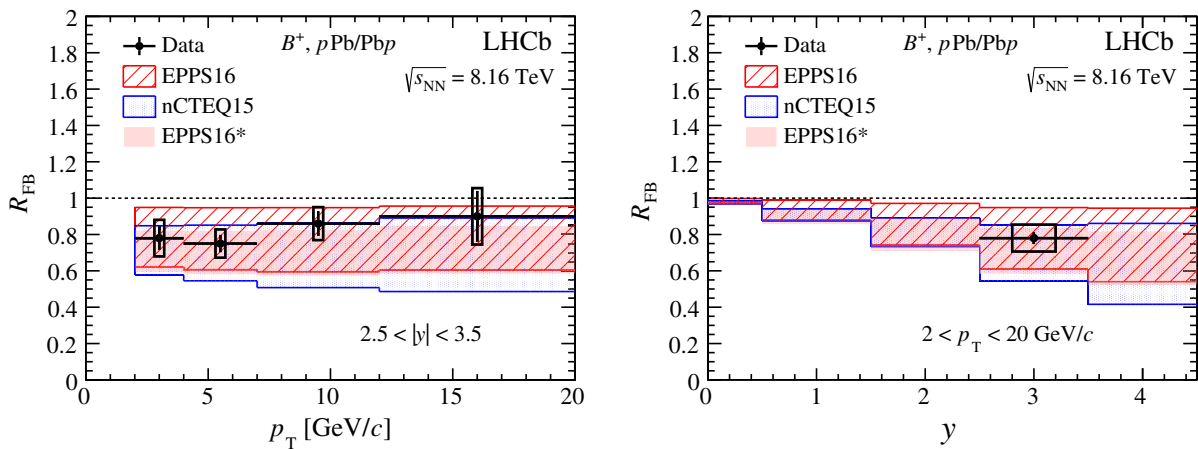
FIG. 9. Forward-backward ratio, R_{FB}, for B^+ mesons as a function of (left) p_T and (right) y in proton-lead collisions compared with HELAC-onia calculations using different nPDF sets. For the data points, the vertical bars (boxes) represent the statistical (total) uncertainties. The rapidity range $2.5 < |y| < 3.5$ represents the common range between the pPb and Pbp data samples studied in this analysis.

TABLE V. Forward-backward ratios, R_{FB}, of B^+, B^0 and Λ_b^0 production in bins of p_T and integrated over $2.5 < |y| < 3.5$. The first uncertainty is statistical and the second systematic.

| $p_T(\text{GeV}/c)$	B^+	B^0	Λ_b^0
(2, 4)	$0.78 \pm 0.06 \pm 0.08$	$0.63 \pm 0.11 \pm 0.12$	$1.14 \pm 0.43 \pm 0.20$
(4, 7)	$0.75 \pm 0.05 \pm 0.06$	$0.78 \pm 0.09 \pm 0.12$	$0.90 \pm 0.15 \pm 0.13$
(7, 12)	$0.86 \pm 0.07 \pm 0.06$	$0.88 \pm 0.10 \pm 0.10$	$0.57 \pm 0.09 \pm 0.06$
(12, 20)	$0.90 \pm 0.14 \pm 0.07$	$0.94 \pm 0.16 \pm 0.10$	$0.89 \pm 0.28 \pm 0.10$
(2, 20)	$0.78 \pm 0.03 \pm 0.07$	$0.75 \pm 0.06 \pm 0.12$	$0.89 \pm 0.12 \pm 0.12$

The R_{FB} ratio as a function of p_T for B^0 mesons and the p_T-integrated value is shown in Fig. 10 and given in Table V. A significant suppression is observed when integrating over the considered p_T range, consistent with the value measured for B^+ mesons. No significant dependence on p_T is seen within the current experimental uncertainties.

In Fig. 11, the forward-backward cross section ratio, R_{FB}, of Λ_b^0 production is shown. The numerical values are summarized in Table V. The observed central value of R_{FB} for the Λ_b^0 baryon is consistent with the measured value for the two b-meson species and with the no-suppression hypothesis. A significant suppression of Λ_b^0 production in pPb data compared to Pbp data is observed for the most precisely measured bin, between 7 and 12 GeV/c. The R_{FB} measurement of Λ_b^0 baryons is consistent with the modifications observed for the beauty mesons within the uncertainties for all kinematic bins. In Fig. 12, the values

FIG. 10. Forward-backward ratio, R_{FB}, of B^0 mesons as a function of (left) p_T and as a function of (right) y in proton-lead collisions. The vertical bars (boxes) represent the statistical (total) uncertainties.

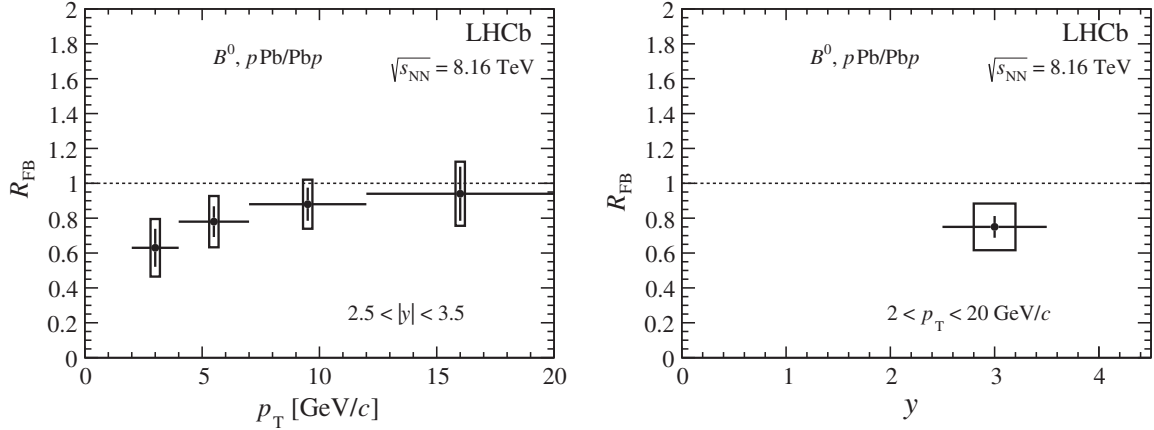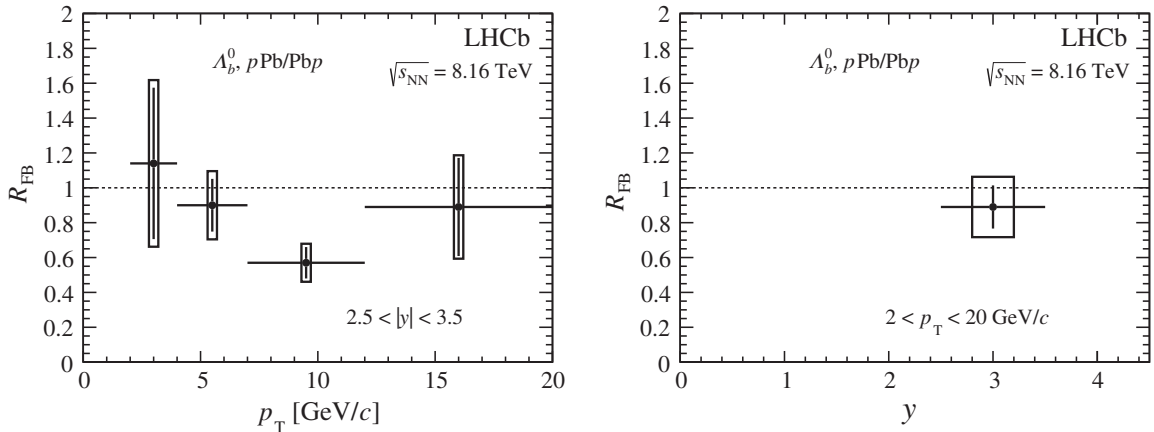

FIG. 11. Forward-backward ratio, R_{FB}, of Λ_b^0 baryons as a function of (left) p_T and (right) y in proton-lead collisions. The vertical bars (boxes) represent the statistical (total) uncertainties.
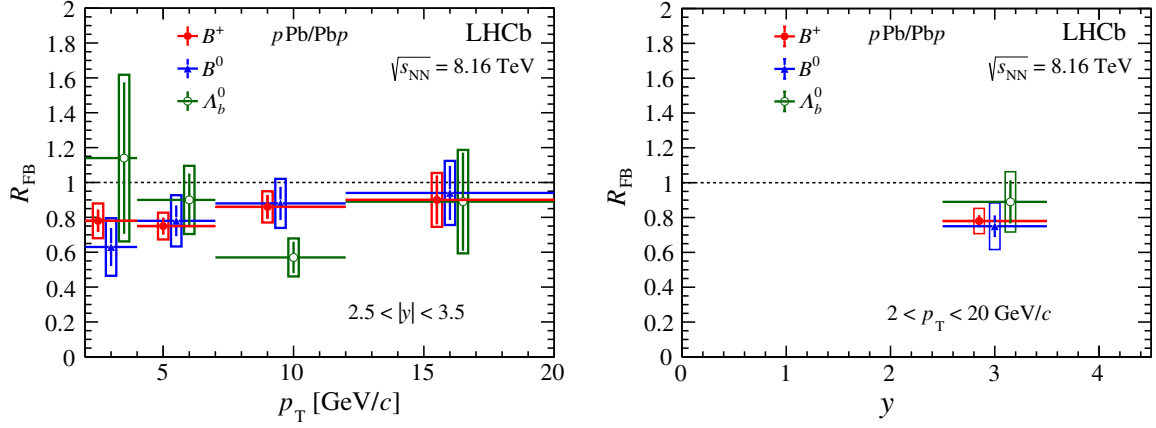
MEASUREMENT OF B^+, B^0 AND Λ_b^0 PRODUCTION IN ...

PHYS. REV. D **99**, 052011 (2019)

FIG. 12. Forward-backward ratio, R_{FB}, of (red) B^+, (blue) B^0 mesons and (green) Λ_b^0 baryons as a function of (left) p_{T} and (right) y in proton-lead collisions. The vertical bars (boxes) represent the statistical (total) uncertainties. Data points are shifted horizontally for better visibility.

of R_{FB} as a function of p_{T} and as a function of y for the three hadrons are compared directly.

C. Nuclear modification factors

In order to gain insight into potential modifications of the b-quark hadronization in pPb and Pbp collisions with respect to pp collisions, the Λ_b^0/B^0 cross section ratio shown in Fig. 8 is divided by the corresponding measurement in pp collisions at $\sqrt{s} = 7$ TeV [23]. Neglecting the dependence on the collision energy of the hadronization with respect to the experimental uncertainties, the quantity corresponds to the ratios of nuclear modification factors

$$R_{p\mathrm{Pb}}^{\Lambda_b^0/B^0} \equiv \frac{R_{p\mathrm{Pb}}^{\Lambda_b^0}}{R_{p\mathrm{Pb}}^{B^0}}. \qquad (4)$$

If the overall nuclear effects for B^0 mesons and Λ_b^0 baryons are identical, $R_{p\mathrm{Pb}}^{\Lambda_b^0/B^0}$ is expected to be unity. This double

ratio is presented as a function of p_{T} and y in Fig. 13 and in Table VI. At positive rapidity, the value of the ratio in all kinematic bins is consistent with unity. At negative rapidity (Pbp), the lowest p_{T} bin exhibits a value smaller than one by more than two standard deviations and the third bin exceeds one by about two standard deviations. The p_{T}-integrated value in the rapidity range $-3.5 < y < -2.5$ is about two standard deviations away from unity. However, more data are required to test whether there are different nuclear effects in beauty mesons and baryons. It would be interesting to check from the theory side whether deviations from unity are expected from models of quark recombination effects in heavy-flavor production in heavy-ion collisions.

The $R_{p\mathrm{Pb}}$ modification factor for B^+ production is shown in Fig. 14, with the numerical values given in Table VII. The values are reported integrated over the considered p_{T} range for the two y intervals, $-3.5 < y < -2.5$ and $2.5 < y < 3.5$. They are also given as a function of p_{T}

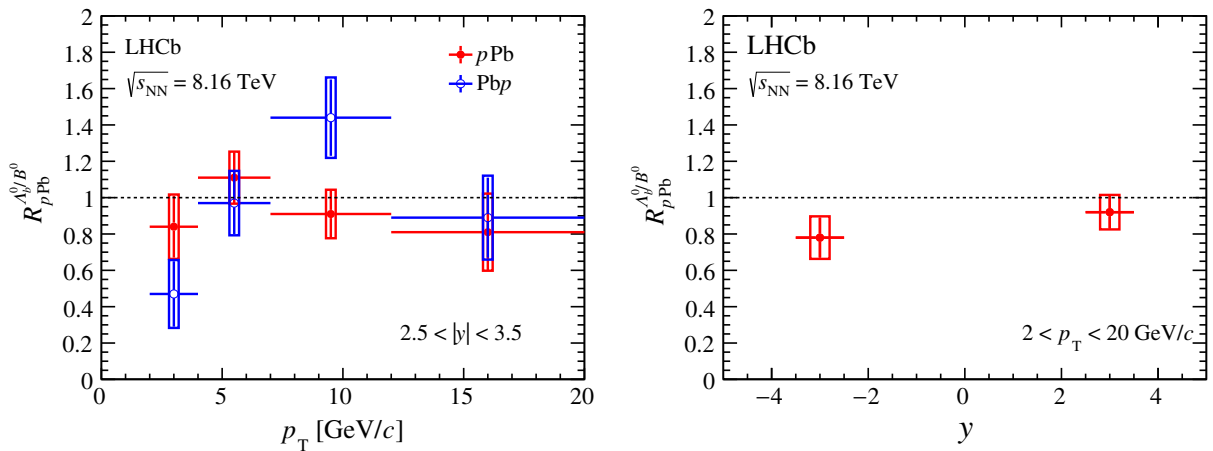FIG. 13. Ratio of nuclear modification factors, $R_{p\mathrm{Pb}}^{\Lambda_b^0/B^0}$, as a function of (left) p_{T} and (right) y in pPb and Pbp collisions. The vertical bars (boxes) represent the statistical (total) uncertainties.

TABLE VI. Ratios of nuclear modification factors, $R_{p\text{Pb}}^{\Lambda_b^0/B^0}$, in bins of p_T and integrated over $2.5 < |y| < 3.5$, for pPb and Pbp samples. The first uncertainty is statistical and the second systematic.

$p_T(\text{GeV}/c)$	pPb	Pbp
(2, 4)	$0.84 \pm 0.17 \pm 0.05$	$0.47 \pm 0.18 \pm 0.05$
(4, 7)	$1.11 \pm 0.14 \pm 0.03$	$0.97 \pm 0.17 \pm 0.05$
(7, 12)	$0.91 \pm 0.13 \pm 0.03$	$1.44 \pm 0.21 \pm 0.07$
(12, 20)	$0.81 \pm 0.21 \pm 0.03$	$0.89 \pm 0.22 \pm 0.07$
(2, 20)	$0.92 \pm 0.09 \pm 0.03$	$0.78 \pm 0.11 \pm 0.04$

TABLE VII. Nuclear modification factor, $R_{p\text{Pb}}$, of B^+ production in pPb and Pbp collisions, in bins of p_T for the range $2.5 < |y| < 3.5$. The first uncertainty is statistical and the second systematic.

$p_T(\text{GeV}/c)$	pPb	Pbp
(2, 4)	$0.75 \pm 0.04 \pm 0.05$	$0.96 \pm 0.06 \pm 0.11$
(4, 7)	$0.77 \pm 0.03 \pm 0.04$	$1.03 \pm 0.05 \pm 0.10$
(7, 12)	$0.83 \pm 0.05 \pm 0.04$	$0.96 \pm 0.05 \pm 0.08$
(12, 20)	$1.01 \pm 0.12 \pm 0.07$	$1.13 \pm 0.12 \pm 0.09$
(2, 20)	$0.78 \pm 0.02 \pm 0.05$	$1.00 \pm 0.03 \pm 0.10$

for both pPb and Pbp collisions. For the pp reference cross section, an interpolation between existing pp cross section measurements by the LHCb collaboration at 7 TeV [54] and 13 TeV [55] is performed. A power-law function is used following the approach of Refs. [17,56,57], which yields a prediction of B^+ production at $\sqrt{s} = 8.16$ TeV consistent with an extrapolation of the measured value at $\sqrt{s} = 7$ TeV using a FONLL calculation [58,59]. The interpolation takes into account the correlations provided in Ref. [55].

The measurement of $R_{p\text{Pb}}$ for nonprompt J/ψ production at the same collision energy by the LHCb collaboration [17] is also shown.

At positive rapidity, a significant suppression by more than 20% is observed integrating over the whole p_T range, whereas at negative rapidity, the result is consistent with unity. The measurement is also consistent with that of nonprompt J/ψ production obtained in a similar kinematic range. The p_T-differential result at positive rapidity shows

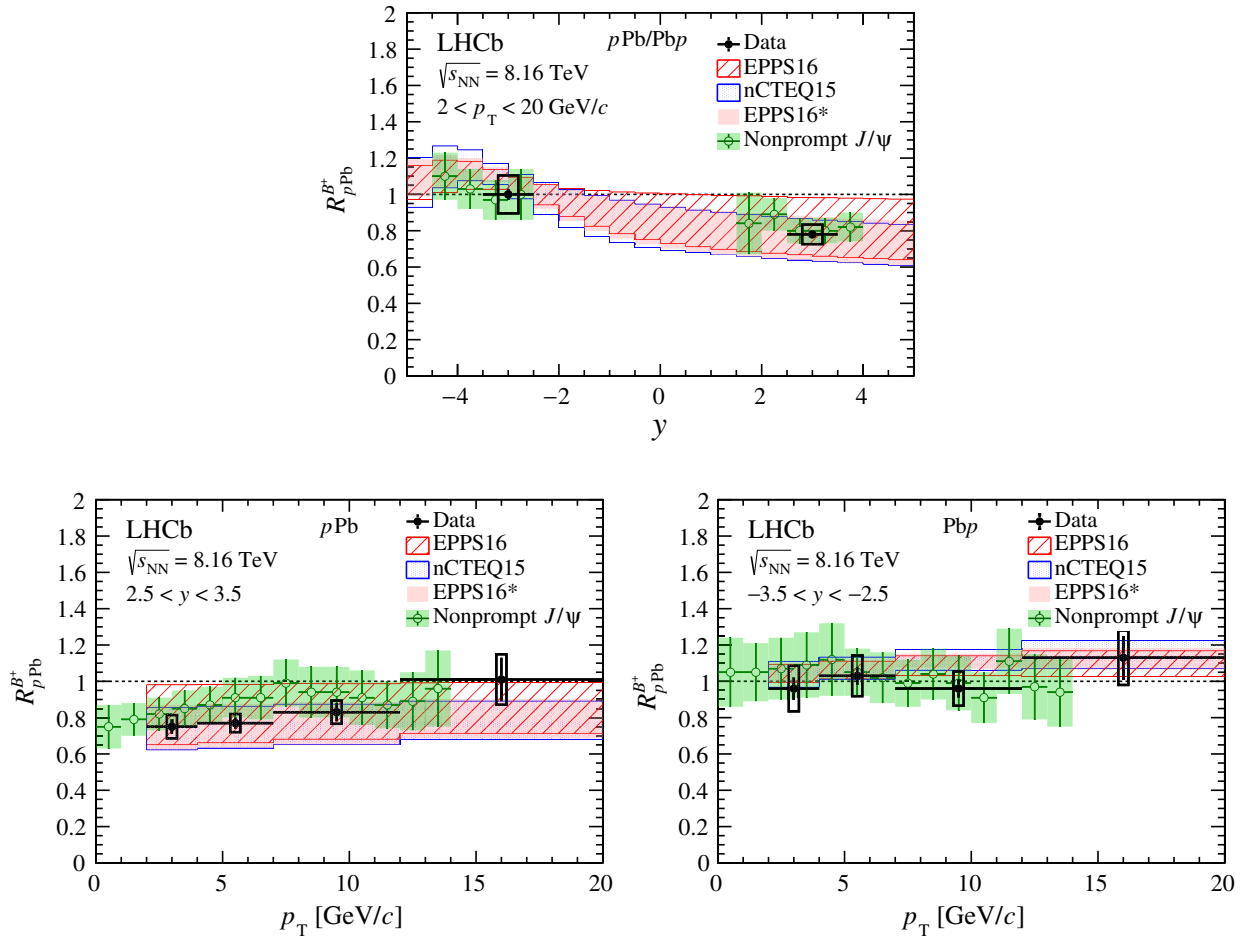FIG. 14. Nuclear modification factor, $R_{p\text{Pb}}$, for B^+ mesons as function of (top) y and as a function of p_T in (bottom left) pPb and (bottom right) Pbp compared with HELAC-onia calculations using different nPDF sets as well as with the measurement of $R_{p\text{Pb}}$ for nonprompt J/ψ production. For the data points, the vertical bars (boxes) represent the statistical (total) uncertainties.

a significant suppression, at the level of 25% for the lowest p_{T} bin. The ratio tends to increase for high p_{T}, however, the current experimental uncertainties that grow also with p_{T} do not allow to establish a significant p_{T} dependence. At negative rapidity, all values are consistent with a nuclear modification factor of one. The experimental data points are in good agreement with the three considered nPDF sets. At positive rapidity, the experimental uncertainties are smaller than the nPDF ones for the integrated values as well as for the three lowest p_{T} bins, whereas the experimental uncertainties are typically larger at negative rapidity. Under the assumption that the dominance of nuclear modification is via nPDFs, the results in the pPb sample provide constraints that can be used in future nPDF fits.

VI. CONCLUSIONS

The differential production cross sections of B^+, B^0 mesons and Λ_b^0 baryons in proton-lead collisions at $\sqrt{s_{\mathrm{NN}}} = 8.16$ TeV are measured in the range $2 < p_{\mathrm{T}} < 20$ GeV/c within the rapidity ranges $1.5 < y < 3.5$ and $-4.5 < y < -2.5$. The cross sections and the derived nuclear modification factors and forward-backward ratios of b-hadron production are measured for the first time with exclusive decay modes at transverse momenta smaller than the mass of the hadrons. They represent the first measurement of beauty-hadron production with different exclusive decay channels in nuclear collisions in that kinematic regime. The results with fully reconstructed beauty hadrons confirm the significant nuclear suppression of beauty-hadron production at positive rapidity measured via nonprompt J/ψ mesons. The observed experimental uncertainties at positive rapidity are smaller than those achieved in a weighting of nPDFs with heavy-flavor data. Therefore, this measurement can serve as a valuable input for future fits of nPDF, assuming that modifications of nPDFs are the dominant source of nuclear effects in proton-lead collisions at the LHC. Finally, the unique measurement of Λ_b^0 production constrains the fragmentation of the beauty quark in a nuclear environment. The baryon-to-meson cross section ratio in proton-lead collisions is found to be compatible with the equivalent ratio measured in pp

collisions, and more data will be needed to study whether nuclear effects modify beauty baryon and meson production differently. These findings are important steps towards a better understanding of heavy-flavor production in nuclear collision systems and will serve as an input for the characterization of the quark-gluon plasma with heavy-flavor observables.

[1] A. Andronic *et al.*, Heavy-flavour and quarkonium production in the LHC era: From proton-proton to heavy-ion collisions, Eur. Phys. J. C **76**, 107 (2016).

[2] M. Bedjidian *et al.*, Heavy flavor physics, arXiv:hep-ph/0311048.

[3] M. Hirai, S. Kumano, and T.-H. Nagai, Determination of nuclear parton distribution functions and their uncertainties in next-to-leading order, Phys. Rev. C **76**, 065207 (2007).

[4] K. J. Eskola, H. Paukkunen, and C. A. Salgado, EPS09: A new generation of NLO and LO nuclear parton distribution functions, J. High Energy Phys. 04 (2009) 065.

[5] D. de Florian, R. Sassot, P. Zurita, and M. Stratmann, Global analysis of nuclear parton distributions, Phys. Rev. D **85**, 074028 (2012).

[6] K. Kovarik *et al.*, nCTEQ15: Global analysis of nuclear parton distributions with uncertainties in

the CTEQ framework, Phys. Rev. D **93**, 085037 (2016).

[7] K. J. Eskola, P. Paakkinen, H. Paukkunen, and C. A. Salgado, EPPS16: Nuclear parton distributions with LHC data, Eur. Phys. J. C **77**, 163 (2017).

[8] F. Gelis, E. Iancu, J. Jalilian-Marian, and R. Venugopalan, The color glass condensate, Annu. Rev. Nucl. Part. Sci. **60**, 463 (2010).

[9] H. Fujii, F. Gelis, and R. Venugopalan, Quark pair production in high energy pA collisions: General features, Nucl. Phys. **A780**, 146 (2006).

[10] F. Arleo and S. Peigné, Heavy-quarkonium suppression in p-A collisions from parton energy loss in cold QCD matter, J. High Energy Phys. 03 (2013) 122.

[11] J. Adam *et al.* (ALICE Collaboration), Enhanced production of multi-strange hadrons in high-multiplicity proton-proton collisions, Nat. Phys. **13**, 535 (2017).

[12] M. Strickland, Small system studies: A theory overview, Nucl. Phys. **A982**, 92 (2019).

[13] S. Acharya *et al.* (ALICE Collaboration), J/ψ Elliptic Flow in Pb-Pb Collisions at $\sqrt{s_{NN}} = 5.02$ TeV, Phys. Rev. Lett. **119**, 242301 (2017).

[14] A. M. Sirunyan *et al.* (CMS Collaboration), Elliptic Flow of Charm and Strange Hadrons in High-Multiplicity pPb Collisions at $\sqrt{s_{NN}} = 8.16$ TeV, Phys. Rev. Lett. **121**, 082301 (2018).

[15] S. Acharya *et al.* (ALICE Collaboration), Λ_c^+ production in pp collisions at $\sqrt{s} = 7$ TeV and in p-Pb collisions at $\sqrt{s_{NN}} = 5.02$ TeV, J. High Energy Phys. 04 (2018) 108.

[16] R. Aaij *et al.* (LHCb Collaboration), Prompt Λ_c^0 production in pPb collisions at $\sqrt{s_{NN}} = 5.02$ TeV, J. High Energy Phys. 02 (2019) 102.

[17] R. Aaij *et al.* (LHCb Collaboration), Prompt and nonprompt J/ψ production and nuclear modification in pPb collisions at $\sqrt{s_{NN}} = 8.16$ TeV, Phys. Lett. B **774**, 159 (2017).

[18] R. Aaij *et al.* (LHCb Collaboration), Study of prompt D^0 meson production in pPb collisions at $\sqrt{s_{NN}} = 5$ TeV, J. High Energy Phys. 10 (**2017**) 090.

[19] A. Kusina, J.-P. Lansberg, I. Schienbein, and H.-S. Shao, Gluon Shadowing in Heavy-Flavor Production at the LHC, Phys. Rev. Lett. **121**, 052004 (2018).

[20] A. Aleedaneshvar and A. N. Khorramian, The impact of the LHCb $B^\pm$ production cross-section on parton distribution functions and determining the mass of heavy quarks, Nucl. Phys. **A979**, 215 (2018).

[21] R. Gauld and J. Rojo, Precision Determination of the Small-x Gluon From Charm Production at LHCb, Phys. Rev. Lett. **118**, 072001 (2017).

[22] R. Aaij *et al.* (LHCb Collaboration), Measurement of the fragmentation fraction ratio f_s/f_d and its dependence on B meson kinematics, J. High Energy Phys. 04 (2013) 001.

[23] R. Aaij *et al.* (LHCb Collaboration), Study of the kinematic dependences of Λ_b^0 production in pp collisions and a measurement of the $\Lambda_b^0 \to \Lambda_c^+ \pi^-$ branching fraction, J. High Energy Phys. 08 (**2014**) 143.

[24] R. Aaij *et al.* (LHCb Collaboration), Measurement of b hadron production fractions in 7 TeV pp collisions, Phys. Rev. D **85**, 032008 (2012).

[25] Y. Zhang, Measurement of heavy flavor production in pp collisions at LHCb, arXiv:1710.04477.

[26] A. A. Alves, Jr. *et al.* (LHCb Collaboration), The LHCb detector at the LHC, J. Instrum. **3**, S08005 (2008).

[27] R. Aaij *et al.* (LHCb Collaboration), LHCb detector performance, Int. J. Mod. Phys. A **30**, 1530022 (2015).

[28] R. Aaij *et al.*, Performance of the LHCb vertex locator, J. Instrum. **9**, P09007 (2014).

[29] P. d'Argent *et al.*, Improved performance of the LHCb outer tracker in LHC Run 2, J. Instrum. **12**, P11016 (2017).

[30] M. Adinolfi *et al.*, Performance of the LHCb RICH detector at the LHC, Eur. Phys. J. C **73**, 2431 (2013).

[31] A. A. Alves, Jr. *et al.*, Performance of the LHCb muon system, J. Instrum. **8**, P02022 (2013).

[32] R. Aaij *et al.*, The LHCb trigger and its performance in 2011, J. Instrum. **8**, P04022 (2013).

[33] G. Dujany and B. Storaci, Real-time alignment and calibration of the LHCb detector in Run II, J. Phys. Conf. Ser. **664**, 082010 (2015).

[34] R. Aaij *et al.*, Tesla: An application for real-time data analysis in high energy physics, Comput. Phys. Commun. **208**, 35 (2016).

[35] T. Pierog, I. Karpenko, J. M. Katzy, E. Yatsenko, and K. Werner, EPOS LHC: Test of collective hadronization with data measured at the CERN large hadron collider, Phys. Rev. C **92**, 034906 (2015).

[36] T. Sjöstrand, S. Mrenna, and P. Skands, A brief introduction to PYTHIA 8.1, Comput. Phys. Commun. **178**, 852 (2008).

[37] T. Sjöstrand, S. Mrenna, and P. Skands, PYTHIA 6.4 physics and manual, J. High Energy Phys. 05 (2006) 026.

[38] D. J. Lange, The EvtGen particle decay simulation package, Nucl. Instrum. Methods Phys. Res., Sect. A **462**, 152 (2001).

[39] P. Golonka and Z. Was, PHOTOS Monte Carlo: A precision tool for QED corrections in Z and W decays, Eur. Phys. J. C **45**, 97 (2006).

[40] J. Allison *et al.* (Geant4 Collaboration), Geant4 developments and applications, IEEE Trans. Nucl. Sci. **53**, 270 (2006); S. Agostinelli *et al.* (Geant4 Collaboration), Geant4: A simulation toolkit, Nucl. Instrum. Methods Phys. Res., Sect. A **506**, 250 (2003).

[41] M. Clemencic, G. Corti, S. Easo, C. R. Jones, S. Miglioranzi, M. Pappagallo, and P. Robbe, The LHCb simulation application, Gauss: Design, evolution and experience, J. Phys. Conf. Ser. **331**, 032023 (2011).

[42] R. Aaij *et al.* (LHCb Collaboration), Precision luminosity measurements at LHCb, J. Instrum. **9**, P12005 (2014).

[43] M. Tanabashi *et al.* (Particle Data Group), Review of particle physics, Phys. Rev. D **98**, 030001 (2018).

[44] M. Pivk and F. R. Le Diberder, sPlot: A statistical tool to unfold data distributions, Nucl. Instrum. Methods Phys. Res., Sect. A **555**, 356 (2005).

[45] T. Skwarnicki, A study of the radiative cascade transitions between the Upsilon-prime and Upsilon resonances, Ph.D. thesis, Institute of Nuclear Physics, Krakow, 1986.

[46] R. Aaij *et al.* (LHCb Collaboration), Measurement of CP observables in $B^\pm \to D^{(*)} K^\pm$ and $B^\pm \to D^{(*)} \pi^\pm$ decays, Phys. Lett. B **777**, 16 (2017).

[47] H. Albrecht *et al.* (ARGUS Collaboration), Search for hadronic $b \to u$ decays, Phys. Lett. B **241**, 278 (1990).

[48] R. Aaij *et al.* (LHCb Collaboration), Measurement of the track reconstruction efficiency at LHCb, J. Instrum. **10**, P02007 (2015).

[49] L. Anderlini *et al.*, The PIDCalib package, Report No. LHCb-PUB-2016-021.

[50] R. Aaij *et al.*, Selection and processing of calibration samples to measure the particle identification performance of the LHCb experiment in Run 2, EPJ Tech. Instrum. **6**, 1 (2019).

[51] H.-S. Shao, HELAC-Onia: An automatic matrix element generator for heavy quarkonium physics, Comput. Phys. Commun. **184**, 2562 (2013).

[52] H.-S. Shao, HELAC-Onia 2.0: An upgraded matrix-element and event generator for heavy quarkonium physics, Comput. Phys. Commun. **198**, 238 (2016).

[53] J.-P. Lansberg and H.-S. Shao, Towards an automated tool to evaluate the impact of the nuclear modification of the gluon density on quarkonium, D and B meson production in proton-nucleus collisions, Eur. Phys. J. C **77**, 1 (2017).

[54] R. Aaij *et al.* (LHCb Collaboration), Measurement of B meson production cross-sections in proton-proton collisions at $\sqrt{s} = 7$ TeV, J. High Energy Phys. 08 (2013) 117.

[55] R. Aaij *et al.* (LHCb Collaboration), Measurement of the $B^{\pm}$ production cross-section in pp collisions at $\sqrt{s} = 7$ and 13 TeV, J. High Energy Phys. 12 (2017) 026.

[56] R. Aaij *et al.* (LHCb Collaboration), Study of J/ψ production and cold nuclear matter effects in pPb collisions at $\sqrt{s_{NN}} = 5$ TeV, J. High Energy Phys. 02 (2014) 072.

[57] R. Aaij *et al.* (LHCb Collaboration), Study of $\psi(2S)$ production cross-sections and cold nuclear matter effects in pPb collisions at $\sqrt{s_{NN}} = 5$ TeV, J. High Energy Phys. 03 (2016) 133.

[58] M. Cacciari, M. Greco, and P. Nason, The p_T spectrum in heavy flavor hadroproduction, J. High Energy Phys. 05 (1998) 007.

[59] M. Cacciari, S. Frixione, N. Houdeau, M. L. Mangano, P. Nason, and G. Ridolfi, Theoretical predictions for charm and bottom production at the LHC, J. High Energy Phys. 10 (2012) 137.

R. Aaij,[29] C. Abellán Beteta,[46] B. Adeva,[43] M. Adinolfi,[50] C. A. Aidala,[77] Z. Ajaltouni,[7] S. Akar,[61] P. Albicocco,[20] J. Albrecht,[12] F. Alessio,[44] M. Alexander,[55] A. Alfonso Albero,[42] G. Alkhazov,[35] P. Alvarez Cartelle,[57] A. A. Alves Jr.,[43] S. Amato,[2] S. Amerio,[25] Y. Amhis,[9] L. An,[19] L. Anderlini,[19] G. Andreassi,[45] M. Andreotti,[18] J. E. Andrews,[62] F. Archilli,[29] J. Arnau Romeu,[8] A. Artamonov,[41] M. Artuso,[63] K. Arzymatov,[39] E. Aslanides,[8] M. Atzeni,[46] B. Audurier,[24] S. Bachmann,[14] J. J. Back,[52] S. Baker,[57] V. Balagura,[9,b] W. Baldini,[18] A. Baranov,[39] R. J. Barlow,[58] G. C. Barrand,[9] S. Barsuk,[9] W. Barter,[57] M. Bartolini,[21] F. Baryshnikov,[73] V. Batozskaya,[33] B. Batsukh,[63] A. Battig,[12] V. Battista,[45] A. Bay,[45] J. Beddow,[55] F. Bedeschi,[26] I. Bediaga,[1] A. Beiter,[63] L. J. Bel,[29] S. Belin,[24] N. Beliy,[4] V. Bellee,[45] N. Belloli,[22,c] K. Belous,[41] I. Belyaev,[36] G. Bencivenni,[20] E. Ben-Haim,[10] S. Benson,[29] S. Beranek,[11] A. Berezhnoy,[37] R. Bernet,[46] D. Berninghoff,[14] E. Bertholet,[10] A. Bertolin,[25] C. Betancourt,[46] F. Betti,[17,44] M. O. Bettler,[51] Ia. Bezshyiko,[46] S. Bhasin,[50] J. Bhom,[31] M. S. Bieker,[12] S. Bifani,[49] P. Billoir,[10] A. Birnkraut,[12] A. Bizzeti,[19,d] M. Bjørn,[59] M. P. Blago,[44] T. Blake,[52] F. Blanc,[45] S. Blusk,[63] D. Bobulska,[55] V. Bocci,[28] O. Boente Garcia,[43] T. Boettcher,[60] A. Bondar,[40,e] N. Bondar,[35] S. Borghi,[58,44] M. Borisyak,[39] M. Borsato,[14] M. Boubdir,[11] T. J. V. Bowcock,[56] C. Bozzi,[18,44] S. Braun,[14] M. Brodski,[44] J. Brodzicka,[31] A. Brossa Gonzalo,[52] D. Brundu,[24,44] E. Buchanan,[50] A. Buonaura,[46] C. Burr,[58] A. Bursche,[24] J. Buytaert,[44] W. Byczynski,[44] S. Cadeddu,[24] H. Cai,[67] R. Calabrese,[18,f] R. Calladine,[49] M. Calvi,[22,c] M. Calvo Gomez,[42,g] A. Camboni,[42,g] P. Campana,[20] D. H. Campora Perez,[44] L. Capriotti,[17,h] A. Carbone,[17,h] G. Carboni,[27] R. Cardinale,[21] A. Cardini,[24] P. Carniti,[22,c] K. Carvalho Akiba,[2] G. Casse,[56] M. Cattaneo,[44] G. Cavallero,[21] R. Cenci,[26,i] D. Chamont,[9] M. G. Chapman,[50] M. Charles,[10] Ph. Charpentier,[44] G. Chatzikonstantinidis,[49] M. Chefdeville,[6] V. Chekalina,[39] C. Chen,[3] S. Chen,[24] S.-G. Chitic,[44] V. Chobanova,[43] M. Chrzaszcz,[44] A. Chubykin,[35] P. Ciambrone,[20] X. Cid Vidal,[43] G. Ciezarek,[44] F. Cindolo,[17] P. E. L. Clarke,[54] M. Clemencic,[44] H. V. Cliff,[51] J. Closier,[44] V. Coco,[44] J. A. B. Coelho,[9] J. Cogan,[8] E. Cogneras,[7] L. Cojocariu,[34] P. Collins,[44] T. Colombo,[44] A. Comerma-Montells,[14] A. Contu,[24] G. Coombs,[44] S. Coquereau,[42] G. Corti,[44] M. Corvo,[18,f] C. M. Costa Sobral,[52] B. Couturier,[44] G. A. Cowan,[54] D. C. Craik,[60] A. Crocombe,[52] M. Cruz Torres,[1] R. Currie,[54] F. Da Cunha Marinho,[2] C. L. Da Silva,[78] E. Dall'Occo,[29] J. Dalseno,[43,j] C. D'Ambrosio,[44] A. Danilina,[36] P. d'Argent,[14] A. Davis,[58] O. De Aguiar Francisco,[44] K. De Bruyn,[44] S. De Capua,[58] M. De Cian,[45] J. M. De Miranda,[1] L. De Paula,[2] M. De Serio,[16,k] P. De Simone,[20] J. A. de Vries,[29] C. T. Dean,[55] W. Dean,[77] D. Decamp,[6] L. Del Buono,[10] B. Delaney,[51] H.-P. Dembinski,[13] M. Demmer,[12] A. Dendek,[32] D. Derkach,[74] O. Deschamps,[7] F. Desse,[9] F. Dettori,[56] B. Dey,[68] A. Di Canto,[44] P. Di Nezza,[20] S. Didenko,[73] H. Dijkstra,[44] F. Dordei,[24] M. Dorigo,[44,l] A. C. dos Reis,[1] A. Dosil Suárez,[43] L. Douglas,[55] A. Dovbnya,[47] K. Dreimanis,[56] L. Dufour,[29] G. Dujany,[10] P. Durante,[44] J. M. Durham,[78] D. Dutta,[58] R. Dzhelyadin,[41,a] M. Dziewiecki,[14] A. Dziurda,[31] A. Dzyuba,[35] S. Easo,[53] U. Egede,[57] V. Egorychev,[36] S. Eidelman,[40,e] S. Eisenhardt,[54] U. Eitschberger,[12] R. Ekelhof,[12] L. Eklund,[55] S. Ely,[63] A. Ene,[34] S. Escher,[11] S. Esen,[29]

T. Evans,[61] A. Falabella,[17] C. Färber,[44] N. Farley,[49] S. Farry,[56] D. Fazzini,[22,44,c] M. Féo,[44] P. Fernandez Declara,[44] A. Fernandez Prieto,[43] F. Ferrari,[17,h] L. Ferreira Lopes,[45] F. Ferreira Rodrigues,[2] M. Ferro-Luzzi,[44] S. Filippov,[38] R. A. Fini,[16] M. Fiorini,[18,f] M. Firlej,[32] C. Fitzpatrick,[45] T. Fiutowski,[32] F. Fleuret,[9,b] M. Fontana,[44] F. Fontanelli,[21,m] R. Forty,[44] V. Franco Lima,[56] M. Frank,[44] C. Frei,[44] J. Fu,[23,n] W. Funk,[44] E. Gabriel,[54] A. Gallas Torreira,[43] D. Galli,[17,h] S. Gallorini,[25] S. Gambetta,[54] Y. Gan,[3] M. Gandelman,[2] P. Gandini,[23] Y. Gao,[3] L. M. Garcia Martin,[76] J. García Pardiñas,[46] B. Garcia Plana,[43] J. Garra Tico,[51] L. Garrido,[42] D. Gascon,[42] C. Gaspar,[44] G. Gazzoni,[7] D. Gerick,[14] E. Gersabeck,[58] M. Gersabeck,[58] T. Gershon,[52] D. Gerstel,[8] Ph. Ghez,[6] V. Gibson,[51] O. G. Girard,[45] P. Gironella Gironell,[42] L. Giubega,[34] K. Gizdov,[54] V. V. Gligorov,[10] C. Göbel,[65] D. Golubkov,[36] A. Golutvin,[57,73] A. Gomes,[1,o] I. V. Gorelov,[37] C. Gotti,[22,c] E. Govorkova,[29] J. P. Grabowski,[14] R. Graciani Diaz,[42] L. A. Granado Cardoso,[44] E. Graugés,[42] E. Graverini,[46] G. Graziani,[19] A. Grecu,[34] R. Greim,[29] P. Griffith,[24] L. Grillo,[58] L. Gruber,[44] B. R. Gruberg Cazon,[59] O. Grünberg,[70] C. Gu,[3] E. Gushchin,[38] A. Guth,[11] Yu. Guz,[41,44] T. Gys,[44] T. Hadavizadeh,[59] C. Hadjivasiliou,[7] G. Haefeli,[45] C. Haen,[44] S. C. Haines,[51] B. Hamilton,[62] X. Han,[14] T. H. Hancock,[59] S. Hansmann-Menzemer,[14] N. Harnew,[59] T. Harrison,[56] C. Hasse,[44] M. Hatch,[44] J. He,[4] M. Hecker,[57] K. Heinicke,[12] A. Heister,[12] K. Hennessy,[56] L. Henry,[76] M. Heß,[70] J. Heuel,[11] A. Hicheur,[64] R. Hidalgo Charman,[58] D. Hill,[59] M. Hilton,[58] P. H. Hopchev,[45] J. Hu,[14] W. Hu,[68] W. Huang,[4] Z. C. Huard,[61] W. Hulsbergen,[29] T. Humair,[57] M. Hushchyn,[74] D. Hutchcroft,[56] D. Hynds,[29] P. Ibis,[12] M. Idzik,[32] P. Ilten,[49] A. Inglessi,[35] A. Inyakin,[41] K. Ivshin,[35] R. Jacobsson,[44] S. Jakobsen,[44] J. Jalocha,[59] E. Jans,[29] B. K. Jashal,[76] A. Jawahery,[62] F. Jiang,[3] M. John,[59] D. Johnson,[44] C. R. Jones,[51] C. Joram,[44] B. Jost,[44] N. Jurik,[59] S. Kandybei,[47] M. Karacson,[44] J. M. Kariuki,[50] S. Karodia,[55] N. Kazeev,[74] M. Kecke,[14] F. Keizer,[51] M. Kelsey,[63] M. Kenzie,[51] T. Ketel,[30] E. Khairullin,[39] B. Khanji,[44] C. Khurewathanakul,[45] K. E. Kim,[63] T. Kirn,[11] V. S. Kirsebom,[45] S. Klaver,[20] K. Klimaszewski,[33] T. Klimkovich,[13] S. Koliiev,[48] M. Kolpin,[14] R. Kopecna,[14] P. Koppenburg,[29] I. Kostiuk,[29,48] S. Kotriakhova,[35] M. Kozeiha,[7] L. Kravchuk,[38] M. Kreps,[52] F. Kress,[57] P. Krokovny,[40,e] W. Krupa,[32] W. Krzemien,[33] W. Kucewicz,[31,p] M. Kucharczyk,[31] V. Kudryavtsev,[40,e] A. K. Kuonen,[45] T. Kvaratskheliya,[36,44] D. Lacarrere,[44] G. Lafferty,[58] A. Lai,[24] D. Lancierini,[46] G. Lanfranchi,[20] C. Langenbruch,[11] T. Latham,[52] C. Lazzeroni,[49] R. Le Gac,[8] R. Lefèvre,[7] A. Leflat,[37] F. Lemaitre,[44] O. Leroy,[8] T. Lesiak,[31] B. Leverington,[14] P.-R. Li,[4,q] Y. Li,[5] Z. Li,[63] X. Liang,[63] T. Likhomanenko,[72] R. Lindner,[44] F. Lionetto,[46] V. Lisovskyi,[9] G. Liu,[66] X. Liu,[3] D. Loh,[52] A. Loi,[24] I. Longstaff,[55] J. H. Lopes,[2] G. Loustau,[46] G. H. Lovell,[51] D. Lucchesi,[25,r] M. Lucio Martinez,[43] Y. Luo,[3] A. Lupato,[25] E. Luppi,[18,f] O. Lupton,[44] A. Lusiani,[26] X. Lyu,[4] F. Machefert,[9] F. Maciuc,[34] V. Macko,[45] P. Mackowiak,[12] S. Maddrell-Mander,[50] O. Maev,[35,44] K. Maguire,[58] D. Maisuzenko,[35] M. W. Majewski,[32] S. Malde,[59] B. Malecki,[44] A. Malinin,[72] T. Maltsev,[40,e] H. Malygina,[14] G. Manca,[24,s] G. Mancinelli,[8] D. Marangotto,[23,n] J. Maratas,[7,t] J. F. Marchand,[6] U. Marconi,[17] C. Marin Benito,[9] M. Marinangeli,[45] P. Marino,[45] J. Marks,[14] P. J. Marshall,[56] G. Martellotti,[28] M. Martinelli,[44] D. Martinez Santos,[43] F. Martinez Vidal,[76] A. Massafferri,[1] M. Materok,[11] R. Matev,[44] A. Mathad,[52] Z. Mathe,[44] C. Matteuzzi,[22] A. Mauri,[46] E. Maurice,[9,b] B. Maurin,[45] M. McCann,[57,44] A. McNab,[58] R. McNulty,[15] J. V. Mead,[56] B. Meadows,[61] C. Meaux,[8] N. Meinert,[70] D. Melnychuk,[33] M. Merk,[29] A. Merli,[23,n] E. Michielin,[25] D. A. Milanes,[69] E. Millard,[52] M.-N. Minard,[6] L. Minzoni,[18,f] D. S. Mitzel,[14] A. Mödden,[12] A. Mogini,[10] R. D. Moise,[57] T. Mombächer,[12] I. A. Monroy,[69] S. Monteil,[7] M. Morandin,[25] G. Morello,[20] M. J. Morello,[26,u] O. Morgunova,[72] J. Moron,[32] A. B. Morris,[8] R. Mountain,[63] F. Muheim,[54] M. Mukherjee,[68] M. Mulder,[29] D. Müller,[44] J. Müller,[12] K. Müller,[46] V. Müller,[12] C. H. Murphy,[59] D. Murray,[58] P. Naik,[50] T. Nakada,[45] R. Nandakumar,[53] A. Nandi,[59] T. Nanut,[45] I. Nasteva,[2] M. Needham,[54] N. Neri,[23,n] S. Neubert,[14] N. Neufeld,[44] R. Newcombe,[57] T. D. Nguyen,[45] C. Nguyen-Mau,[45,v] S. Nieswand,[11] R. Niet,[12] N. Nikitin,[37] A. Nogay,[72] N. S. Nolte,[44] A. Oblakowska-Mucha,[32] V. Obraztsov,[41] S. Ogilvy,[55] D. P. O'Hanlon,[17] R. Oldeman,[24,s] C. J. G. Onderwater,[71] A. Ossowska,[31] J. M. Otalora Goicochea,[2] T. Ovsiannikova,[36] P. Owen,[46] A. Oyanguren,[76] P. R. Pais,[45] T. Pajero,[26,u] A. Palano,[16] M. Palutan,[20] G. Panshin,[75] A. Papanestis,[53] M. Pappagallo,[54] L. L. Pappalardo,[18,f] W. Parker,[62] C. Parkes,[58,44] G. Passaleva,[19,44] A. Pastore,[16] M. Patel,[57] C. Patrignani,[17,h] A. Pearce,[44] A. Pellegrino,[29] G. Penso,[28] M. Pepe Altarelli,[44] S. Perazzini,[44] D. Pereima,[36] P. Perret,[7] L. Pescatore,[45] K. Petridis,[50] A. Petrolini,[21,m] A. Petrov,[72] S. Petrucci,[54] M. Petruzzo,[23,n] B. Pietrzyk,[6] G. Pietrzyk,[45] M. Pikies,[31] M. Pili,[59] D. Pinci,[28] J. Pinzino,[44] F. Pisani,[44] A. Piucci,[14] V. Placinta,[34] S. Playfer,[54] J. Plews,[49] M. Plo Casasus,[43] F. Polci,[10] M. Poli Lener,[20] A. Poluektov,[8] N. Polukhina,[73,w] I. Polyakov,[63] E. Polycarpo,[2] G. J. Pomery,[50] S. Ponce,[44] A. Popov,[41] D. Popov,[49,13] S. Poslavskii,[41] E. Price,[50] J. Prisciandaro,[43] C. Prouve,[43] V. Pugatch,[48] A. Puig Navarro,[46] H. Pullen,[59] G. Punzi,[26,i] W. Qian,[4] J. Qin,[4] R. Quagliani,[10] B. Quintana,[7] N. V. Raab,[15] B. Rachwal,[32] J. H. Rademacker,[50] M. Rama,[26] M. Ramos Pernas,[43] M. S. Rangel,[2] F. Ratnikov,[39,74] G. Raven,[30] M. Ravonel Salzgeber,[44] M. Reboud,[6] F. Redi,[45] S. Reichert,[12] F. Reiss,[10] C. Remon Alepuz,[76]

Z. Ren,[3] V. Renaudin,[59] S. Ricciardi,[53] S. Richards,[50] K. Rinnert,[56] P. Robbe,[9] A. Robert,[10] A. B. Rodrigues,[45] E. Rodrigues,[61] J. A. Rodriguez Lopez,[69] M. Roehrken,[44] S. Roiser,[44] A. Rollings,[59] V. Romanovskiy,[41] A. Romero Vidal,[43] J. D. Roth,[77] M. Rotondo,[20] M. S. Rudolph,[63] T. Ruf,[44] J. Ruiz Vidal,[76] J. J. Saborido Silva,[43] N. Sagidova,[35] B. Saitta,[24,s] V. Salustino Guimaraes,[65] C. Sanchez Gras,[29] C. Sanchez Mayordomo,[76] B. Sanmartin Sedes,[43] R. Santacesaria,[28] C. Santamarina Rios,[43] M. Santimaria,[20,44] E. Santovetti,[27,x] G. Sarpis,[58] A. Sarti,[20,y] C. Satriano,[28,z] A. Satta,[27] M. Saur,[4] D. Savrina,[36,37] S. Schael,[11] M. Schellenberg,[12] M. Schiller,[55] H. Schindler,[44] M. Schmelling,[13] T. Schmelzer,[12] B. Schmidt,[44] O. Schneider,[45] A. Schopper,[44] H. F. Schreiner,[61] M. Schubiger,[45] S. Schulte,[45] M. H. Schune,[9] R. Schwemmer,[44] B. Sciascia,[20] A. Sciubba,[28,y] A. Semennikov,[36] E. S. Sepulveda,[10] A. Sergi,[49] N. Serra,[46] J. Serrano,[8] L. Sestini,[25] A. Seuthe,[12] P. Seyfert,[44] M. Shapkin,[41] T. Shears,[56] L. Shekhtman,[40,e] V. Shevchenko,[72] E. Shmanin,[73] B. G. Siddi,[18] R. Silva Coutinho,[46] L. Silva de Oliveira,[2] G. Simi,[25,r] S. Simone,[16,k] I. Skiba,[18] N. Skidmore,[14] T. Skwarnicki,[63] M. W. Slater,[49] J. G. Smeaton,[51] E. Smith,[11] I. T. Smith,[54] M. Smith,[57] M. Soares,[17] l. Soares Lavra,[1] M. D. Sokoloff,[61] F. J. P. Soler,[55] B. Souza De Paula,[2] B. Spaan,[12] E. Spadaro Norella,[23,n] P. Spradlin,[55] F. Stagni,[44] M. Stahl,[14] S. Stahl,[44] P. Stefko,[45] S. Stefkova,[57] O. Steinkamp,[46] S. Stemmle,[14] O. Stenyakin,[41] M. Stepanova,[35] H. Stevens,[12] A. Stocchi,[9] S. Stone,[63] B. Storaci,[46] S. Stracka,[26] M. E. Stramaglia,[45] M. Straticiuc,[34] U. Straumann,[46] S. Strokov,[75] J. Sun,[3] L. Sun,[67] Y. Sun,[62] K. Swientek,[32] A. Szabelski,[33] T. Szumlak,[32] M. Szymanski,[4] Z. Tang,[3] T. Tekampe,[12] G. Tellarini,[18] F. Teubert,[44] E. Thomas,[44] M. J. Tilley,[57] V. Tisserand,[7] S. T'Jampens,[6] M. Tobin,[32] S. Tolk,[44] L. Tomassetti,[18,f] D. Tonelli,[26] D. Y. Tou,[10] R. Tourinho Jadallah Aoude,[1] E. Tournefier,[6] M. Traill,[55] M. T. Tran,[45] A. Trisovic,[51] A. Tsaregorodtsev,[8] G. Tuci,[26,i] A. Tully,[51] N. Tuning,[29,44] A. Ukleja,[33] A. Usachov,[9] A. Ustyuzhanin,[39,74] U. Uwer,[14] A. Vagner,[75] V. Vagnoni,[17] A. Valassi,[44] S. Valat,[44] G. Valenti,[17] M. van Beuzekom,[29] E. van Herwijnen,[44] J. van Tilburg,[29] M. van Veghel,[29] R. Vazquez Gomez,[44] P. Vazquez Regueiro,[43] C. Vázquez Sierra,[29] S. Vecchi,[18] J. J. Velthuis,[50] M. Veltri,[19,aa] A. Venkateswaran,[63] M. Vernet,[7] M. Veronesi,[29] M. Vesterinen,[52] J. V. Viana Barbosa,[44] D. Vieira,[4] M. Vieites Diaz,[43] H. Viemann,[70] X. Vilasis-Cardona,[42,g] A. Vitkovskiy,[29] M. Vitti,[51] V. Volkov,[37] A. Vollhardt,[46] D. Vom Bruch,[10] B. Voneki,[44] A. Vorobyev,[35] V. Vorobyev,[40,e] N. Voropaev,[35] R. Waldi,[70] J. Walsh,[26] J. Wang,[5] M. Wang,[3] Y. Wang,[68] Z. Wang,[46] D. R. Ward,[51] H. M. Wark,[56] N. K. Watson,[49] D. Websdale,[57] A. Weiden,[46] C. Weisser,[60] M. Whitehead,[11] G. Wilkinson,[59] M. Wilkinson,[63] I. Williams,[51] M. Williams,[60] M. R. J. Williams,[58] T. Williams,[49] F. F. Wilson,[53] M. Winn,[9] W. Wislicki,[33] M. Witek,[31] G. Wormser,[9] S. A. Wotton,[51] K. Wyllie,[44] D. Xiao,[68] Y. Xie,[68] A. Xu,[3] M. Xu,[68] Q. Xu,[4] Z. Xu,[6] Z. Xu,[3] Z. Yang,[3] Z. Yang,[62] Y. Yao,[63] L. E. Yeomans,[56] H. Yin,[68] J. Yu,[68,bb] X. Yuan,[63] O. Yushchenko,[41] K. A. Zarebski,[49] M. Zavertyaev,[13,w] D. Zhang,[68] L. Zhang,[3] W. C. Zhang,[3,cc] Y. Zhang,[44] A. Zhelezov,[14] Y. Zheng,[4] X. Zhu,[3] V. Zhukov,[11,37] J. B. Zonneveld,[54] and S. Zucchelli[17,h]

(LHCb Collaboration)

[1]Centro Brasileiro de Pesquisas Físicas (CBPF), Rio de Janeiro, Brazil
[2]Universidade Federal do Rio de Janeiro (UFRJ), Rio de Janeiro, Brazil
[3]Center for High Energy Physics, Tsinghua University, Beijing, China
[4]University of Chinese Academy of Sciences, Beijing, China
[5]Institute Of High Energy Physics (ihep), Beijing, China
[6]Univ. Grenoble Alpes, Univ. Savoie Mont Blanc, CNRS, IN2P3-LAPP, Annecy, France
[7]Université Clermont Auvergne, CNRS/IN2P3, LPC, Clermont-Ferrand, France
[8]Aix Marseille Univ, CNRS/IN2P3, CPPM, Marseille, France
[9]LAL, Univ. Paris-Sud, CNRS/IN2P3, Université Paris-Saclay, Orsay, France
[10]LPNHE, Sorbonne Université, Paris Diderot Sorbonne Paris Cité, CNRS/IN2P3, Paris, France
[11]I. Physikalisches Institut, RWTH Aachen University, Aachen, Germany
[12]Fakultät Physik, Technische Universität Dortmund, Dortmund, Germany
[13]Max-Planck-Institut für Kernphysik (MPIK), Heidelberg, Germany
[14]Physikalisches Institut, Ruprecht-Karls-Universität Heidelberg, Heidelberg, Germany
[15]School of Physics, University College Dublin, Dublin, Ireland
[16]INFN Sezione di Bari, Bari, Italy
[17]INFN Sezione di Bologna, Bologna, Italy
[18]INFN Sezione di Ferrara, Ferrara, Italy
[19]INFN Sezione di Firenze, Firenze, Italy
[20]INFN Laboratori Nazionali di Frascati, Frascati, Italy
[21]INFN Sezione di Genova, Genova, Italy

[22]INFN Sezione di Milano-Bicocca, Milano, Italy
[23]INFN Sezione di Milano, Milano, Italy
[24]INFN Sezione di Cagliari, Monserrato, Italy
[25]INFN Sezione di Padova, Padova, Italy
[26]INFN Sezione di Pisa, Pisa, Italy
[27]INFN Sezione di Roma Tor Vergata, Roma, Italy
[28]INFN Sezione di Roma La Sapienza, Roma, Italy
[29]Nikhef National Institute for Subatomic Physics, Amsterdam, Netherlands
[30]Nikhef National Institute for Subatomic Physics and VU University Amsterdam, Amsterdam, Netherlands
[31]Henryk Niewodniczanski Institute of Nuclear Physics Polish Academy of Sciences, Kraków, Poland
[32]AGH—University of Science and Technology, Faculty of Physics and Applied Computer Science,
Kraków, Poland
[33]National Center for Nuclear Research (NCBJ), Warsaw, Poland
[34]Horia Hulubei National Institute of Physics and Nuclear Engineering, Bucharest-Magurele, Romania
[35]Petersburg Nuclear Physics Institute (PNPI), Gatchina, Russia
[36]Institute of Theoretical and Experimental Physics (ITEP), Moscow, Russia
[37]Institute of Nuclear Physics, Moscow State University (SINP MSU), Moscow, Russia
[38]Institute for Nuclear Research of the Russian Academy of Sciences (INR RAS), Moscow, Russia
[39]Yandex School of Data Analysis, Moscow, Russia
[40]Budker Institute of Nuclear Physics (SB RAS), Novosibirsk, Russia
[41]Institute for High Energy Physics (IHEP), Protvino, Russia
[42]ICCUB, Universitat de Barcelona, Barcelona, Spain
[43]Instituto Galego de Física de Altas Enerxías (IGFAE), Universidade de Santiago de Compostela,
Santiago de Compostela, Spain
[44]European Organization for Nuclear Research (CERN), Geneva, Switzerland
[45]Institute of Physics, Ecole Polytechnique Fédérale de Lausanne (EPFL), Lausanne, Switzerland
[46]Physik-Institut, Universität Zürich, Zürich, Switzerland
[47]NSC Kharkiv Institute of Physics and Technology (NSC KIPT), Kharkiv, Ukraine
[48]Institute for Nuclear Research of the National Academy of Sciences (KINR), Kyiv, Ukraine
[49]University of Birmingham, Birmingham, United Kingdom
[50]H.H. Wills Physics Laboratory, University of Bristol, Bristol, United Kingdom
[51]Cavendish Laboratory, University of Cambridge, Cambridge, United Kingdom
[52]Department of Physics, University of Warwick, Coventry, United Kingdom
[53]STFC Rutherford Appleton Laboratory, Didcot, United Kingdom
[54]School of Physics and Astronomy, University of Edinburgh, Edinburgh, United Kingdom
[55]School of Physics and Astronomy, University of Glasgow, Glasgow, United Kingdom
[56]Oliver Lodge Laboratory, University of Liverpool, Liverpool, United Kingdom
[57]Imperial College London, London, United Kingdom
[58]School of Physics and Astronomy, University of Manchester, Manchester, United Kingdom
[59]Department of Physics, University of Oxford, Oxford, United Kingdom
[60]Massachusetts Institute of Technology, Cambridge, Massachusetts, USA
[61]University of Cincinnati, Cincinnati, Ohio, USA
[62]University of Maryland, College Park, Maryland, USA
[63]Syracuse University, Syracuse, New York, USA
[64]Laboratory of Mathematical and Subatomic Physics, Constantine, Algeria
(associated with Universidade Federal do Rio de Janeiro (UFRJ), Rio de Janeiro, Brazil)
[65]Pontifícia Universidade Católica do Rio de Janeiro (PUC-Rio), Rio de Janeiro, Brazil
(associated with Universidade Federal do Rio de Janeiro (UFRJ), Rio de Janeiro, Brazil)
[66]South China Normal University, Guangzhou, China
(associated with Center for High Energy Physics, Tsinghua University, Beijing, China)
[67]School of Physics and Technology, Wuhan University, Wuhan, China
(associated with Center for High Energy Physics, Tsinghua University, Beijing, China)
[68]Institute of Particle Physics, Central China Normal University, Wuhan, Hubei, China
(associated with Center for High Energy Physics, Tsinghua University, Beijing, China)
[69]Departamento de Fisica, Universidad Nacional de Colombia, Bogota, Colombia
(associated with LPNHE, Sorbonne Université, Paris Diderot Sorbonne Paris Cité, CNRS/IN2P3,
Paris, France)
[70]Institut für Physik, Universität Rostock, Rostock, Germany
(associated with Physikalisches Institut, Ruprecht-Karls-Universität Heidelberg, Heidelberg, Germany)

^{71}*Van Swinderen Institute, University of Groningen, Groningen, Netherlands*
(associated with Nikhef National Institute for Subatomic Physics, Amsterdam, Netherlands)
^{72}*National Research Centre Kurchatov Institute, Moscow, Russia*
(associated with Institute of Theoretical and Experimental Physics (ITEP), Moscow, Russia)
^{73}*National University of Science and Technology "MISIS", Moscow, Russia*
(associated with Institute of Theoretical and Experimental Physics (ITEP), Moscow, Russia)
^{74}*National Research University Higher School of Economics, Moscow, Russia*
(associated with Yandex School of Data Analysis, Moscow, Russia)
^{75}*National Research Tomsk Polytechnic University, Tomsk, Russia*
(associated with Institute of Theoretical and Experimental Physics (ITEP), Moscow, Russia)
^{76}*Instituto de Fisica Corpuscular, Centro Mixto Universidad de Valencia—CSIC, Valencia, Spain*
(associated with ICCUB, Universitat de Barcelona, Barcelona, Spain)
^{77}*University of Michigan, Ann Arbor, Michigan, USA*
(associated with Syracuse University, Syracuse, New York, USA)
^{78}*Los Alamos National Laboratory (LANL), Los Alamos, United States*
(associated with Syracuse University, Syracuse, New York, USA)

[a]Deceased.
[b]Also at Laboratoire Leprince-Ringuet, Palaiseau, France.
[c]Also at Università di Milano Bicocca, Milano, Italy.
[d]Also at Università di Modena e Reggio Emilia, Modena, Italy.
[e]Also at Novosibirsk State University, Novosibirsk, Russia.
[f]Also at Università di Ferrara, Ferrara, Italy.
[g]Also at LIFAELS, La Salle, Universitat Ramon Llull, Barcelona, Spain.
[h]Also at Università di Bologna, Bologna, Italy.
[i]Also at Università di Pisa, Pisa, Italy.
[j]Also at H.H. Wills Physics Laboratory, University of Bristol, Bristol, United Kingdom.
[k]Also at Università di Bari, Bari, Italy.
[l]Also at Sezione INFN di Trieste, Trieste, Italy.
[m]Also at Università di Genova, Genova, Italy.
[n]Also at Università degli Studi di Milano, Milano, Italy.
[o]Also at Universidade Federal do Triângulo Mineiro (UFTM), Uberaba-MG, Brazil.
[p]Also at AGH—University of Science and Technology, Faculty of Computer Science, Electronics and Telecommunications, Kraków, Poland.
[q]Also at Lanzhou University, Lanzhou, China.
[r]Also at Università di Padova, Padova, Italy.
[s]Also at Università di Cagliari, Cagliari, Italy.
[t]Also at MSU—Iligan Institute of Technology (MSU-IIT), Iligan, Philippines.
[u]Also at Scuola Normale Superiore, Pisa, Italy.
[v]Also at Hanoi University of Science, Hanoi, Vietnam.
[w]Also at P.N. Lebedev Physical Institute, Russian Academy of Science (LPI RAS), Moscow, Russia.
[x]Also at Università di Roma Tor Vergata, Roma, Italy.
[y]Also at Università di Roma La Sapienza, Roma, Italy.
[z]Also at Università della Basilicata, Potenza, Italy.
[aa]Also at Università di Urbino, Urbino, Italy.
[bb]Also at Physics and Micro Electronic College, Hunan University, Changsha City, China.
[cc]Also at School of Physics and Information Technology, Shaanxi Normal University (SNNU), Xi'an, China.